

Generating metal-polluting debris in white dwarf planetary systems from small-impact crater ejecta

Dimitri Veras^{1,2*†}, Kosuke Kurosawa³

¹*Centre for Exoplanets and Habitability, University of Warwick, Coventry CV4 7AL, UK*

²*Department of Physics, University of Warwick, Coventry CV4 7AL, UK*

³*Planetary Exploration Research Center, Chiba Institute of Technology, 2-17-1, Narashino, Tsudanuma, Chiba 275-0016, Japan*

12 January 2022

ABSTRACT

Metal pollution in white dwarf photospheres originates from the accretion of some combination of planets, moons, asteroids, comets, boulders, pebbles and dust. When large bodies reside in dynamically stagnant locations – unable themselves to pollute nor even closely approach the white dwarf – then smaller reservoirs of impact debris may become a complementary or the primary source of metal pollutants. Here, we take a first step towards exploring this possibility by computing limits on the recoil mass that escapes the gravitational pull of the target object following a single impact onto an atmosphere-less surface. By considering vertical impacts only with the full-chain analytical prescription from Kurosawa & Takada (2019), we provide lower bounds for the ejected mass for basalt, granite, iron and water-rich target objects across the radii range 10^0 – 3 km. Our use of the full-chain prescription as opposed to physical experiments or hydrocode simulations allows us to quickly sample a wide range of parameter space appropriate to white dwarf planetary systems. Our numerical results could be used in future studies to constrain freshly-generated small debris reservoirs around white dwarfs given a particular planetary system architecture, bombardment history, and impact geometries.

Key words: minor planets, asteroids: general – stars: white dwarfs – planets and satellites: surfaces – celestial mechanics – planet and satellites: dynamical evolution and stability – protoplanetary discs

1 INTRODUCTION

1.1 Fates of planetary systems

As the endpoint of stellar evolution for the majority of stars in the Galaxy, white dwarfs showcase the fate of planetary systems. Our Sun will become a white dwarf, and will likely host five or six major planets that will have managed to survive the intermediate giant branch phase of Solar evolution (Schröder & Smith 2008; Veras 2016a; Schreiber et al. 2019). The Solar white dwarf will also host moons, comets, asteroids, boulders, pebbles and dust.

Radiative forces and dynamical instability amongst these objects could lead some to migrate towards and accrete onto the solar white dwarf (Veras 2016b). Because white dwarfs have surface gravities which are 10^5 higher than the Earth’s, white dwarf atmospheres chemically stratify this accreted matter (Schatzman 1958; Paquette et al. 1986; Koester 2009).

1.1.1 Chemistry of white dwarf metal pollution

Because white dwarf atmospheres are composed exclusively of hydrogen, helium or some combination of the two, accreted planetary material is easily distinguished¹, and regularly observed from both the ground (Dufour et al. 2007, Klein et al. 2010, 2011, Kleinman et al. 2013, Wilson et al. 2014, Gentile Fusillo et al. 2015, Kepler et al. 2015, 2016, Hollands et al. 2017, 2018) and from space (Gänsicke et al. 2012, Jura et al. 2012, Xu et al. 2013, 2014, Wilson et al. 2015, 2016, Melis & Dufour 2017, Coutu et al. 2019). As a result, we can extract the bulk chemical composition of exo-planetary bodies by observing their broken-up remains (Jura & Young 2014). These autopsies represent the only direct currently available means to probe rocky interiors.

The above studies and others have so far yielded the detection of the following 20 metals (with atomic num-

¹ Any fallback material from the progenitor’s stellar winds would sink at too early of an epoch to be observed and is anyway compositionally dis-similar from accreted planetary material.

* E-mail: d.veras@warwick.ac.uk
† STFC Ernest Rutherford Fellow

ber): C(6), N(7), O(8), Na(11), Mg(12), Al(13), Si(14), P(15), S(16), Ca(20), Sc(21), Ti(22), V(23), Cr(24), Mn(25), Fe(26), Co(27), Ni(28), Cu(29) and Sr(38). Nearly all polluted white dwarfs contain either Ca or Mg, which generate the strongest spectral signatures; in contrast, for only one white dwarf has N been detected (Xu et al. 2017). Some white dwarfs contain at least ten different observable exoplanetary metals (e.g. Dufour et al. 2012; Melis & Dufour 2017; Swan et al. 2019; Xu et al. 2019), and about two dozen white dwarfs currently host at least five metals (Harrison et al. 2018; Hollands et al. 2018). In each case, because of spectroscopic limitations, we obtain only a partial snapshot of the bulk chemical composition of progenitor exoplanetary material.

Overall, the ensemble of metals found in white dwarf atmospheres is indicative of dry (volatile-poor) progenitors with compositions similar to the bulk Earth (Gänsicke et al. 2012; Jura & Young 2014; Harrison et al. 2018; Hollands et al. 2018; Zuckerman & Young 2018; Doyle et al. 2019; Bonsor et al. 2020). Determining if the composition of the surrounding debris and gas matches that of the metal pollution is challenging², and so far has yielded constraints in just a few cases: for the close and bright G29-38 (Reach et al. 2005, 2009), the minor planet host WD 1145+017 (Xu et al. 2016; Cauley et al. 2018; Fortin-Archambault et al. 2020) and the major planet host WD J0914+1914 (Gänsicke et al. 2019). Nevertheless, the above evidence for volatile-poor atmospheric pollution is overwhelming. Therefore in this paper, the consideration of a terrestrial-like composition (at least with granite or basalt) is paramount.

Some white dwarfs, however, showcase high-profile exceptions. In a few instances, the progenitors were volatile-rich and were composed of water by mass fractions of tens of per cent (Farihi et al. 2013; Raddi et al. 2015; Gentile Fusillo et al. 2017; Xu et al. 2017). These observations are supported by theoretical studies which have quantified how internal water can be retained even during the giant branch phases of stellar evolution (Malamud & Perets 2016, 2017a,b). Hence, in this paper we also consider water-rich bodies. Finally, one polluted white dwarf was recently shown to be orbited by a ferrous core fragment (Manser et al. 2019), indicating the importance of modelling iron-rich bodies, which we also consider here.

We therefore choose basalt, granite, water and iron in this paper as representations of exoplanetary material solely based on white dwarf metal pollution. White dwarf pollution provides the most direct way of measuring exoplanetary bulk chemical compositions, because observational data on major exoplanets is, at best, otherwise largely restricted to their masses and radii only. Although a handful of chemical elements and molecules have been positively detected in main-sequence exoplanetary atmospheres, these elements do not necessarily reflect the planets' bulk chemical compositions, and plane-

tary atmospheric composition would change in time with white dwarf cooling (Kozakis et al. 2018). Other potential future avenues for complementing the chemical constraints from pollution include linking main-sequence stellar composition with planet formation (Santos et al. 2017; Hinkel & Unterborn 2018; Kunitomo et al. 2018; Liu et al. 2018; Cabral et al. 2019) and detecting chemical elements in sublimated tails of closely orbiting disintegrating bodies (van Lieshout et al. 2014; Bodman et al. 2018; Colón et al. 2018; Ridden-Harper et al. 2019).

1.1.2 Dynamics of white dwarf metal pollution

The chemical constraints above, in addition to dynamical considerations, support the canonical assumption that the accreted material primarily arises from exo-asteroids as opposed to other classes of extrasolar bodies.

Several observational and theoretical studies reinforce this conclusion. An exo-asteroid is currently observed to be disintegrating while orbiting the white dwarf WD 1145+017 at its Roche radius (Vanderburg et al. 2015), and other ones are thought to be producing the debris around ZTF J0139+5245 (Vanderbosch et al. 2019). The dynamical origin of these bodies are unknown, but may have been captured by extant extended discs of gas (Grishin & Veras 2019). Additionally, full-lifetime dynamical simulations including the interaction between exoplanets and exo-asteroids (Mustill et al. 2018) have successfully demonstrated that the latter is accreted onto the white dwarf at a frequency which is commensurate with observations (Hollands et al. 2018). Systems with few exo-asteroids can still produce pollution over prolonged timescales through chaotic self-disruption en route to the white dwarf on high-eccentricity orbits, providing intermittent streams of polluting material (Makarov & Veras 2019; Veras et al. 2020a).

Other types of polluters may occasionally contribute to the metal budget in white dwarf atmospheres. An exo-planet breaking up around a white dwarf (Malamud & Perets 2020a,b) and accreting onto the star would showcase a much stronger observational signature than an exo-asteroid which suffers the same fate (Bear & Soker 2013, 2015). However, despite the exciting discovery of an ice giant in a compact orbit around a white dwarf (Gänsicke et al. 2019), exo-planets are not numerous enough for their destruction to occur at a high-enough frequency (Debes & Sigurdsson 2002; Veras et al. 2013; Voyatzis et al. 2013; Mustill et al. 2014; Veras & Gänsicke 2015; Veras et al. 2016, 2018a) to match the fraction (25-50 per cent) of the observable Milky Way single white dwarfs which feature metal pollution (Zuckerman et al. 2003, 2010; Koester et al. 2014).

Exo-moons which experience post-main-sequence evolution can be stripped from their parent exo-planets and then collide with the white dwarf (Payne et al. 2016, 2017). However, like exo-planets, exo-moons are not numerous enough (at least if our solar system moons are representative) to explain widespread metal pollution.

An exo-Oort cloud comet, on average, will impact a white dwarf every 10^4 yr (Alcock et al. 1986; Veras et al. 2014a), providing only a secondary contribution to accreted metals. This statement holds true even if this value varies significantly based on different models and assumptions

² Around younger, main-sequence stars, IR observations have revolutionized the fields of planet formation (see reviews by Wyatt 2008, Kral et al. 2018 and Andrews 2020), although determining grain composition from these observations remains nuanced.

(Parriott & Alcock 1998; Stone et al. 2015; Caiazzo & Heyl 2017).

1.1.3 Small body reservoirs

The reservoirs of bodies smaller than exo-asteroids, however, remain largely unexplored. Some of these reservoirs will carry over from the giant branch phase of stellar evolution (Bonsor & Wyatt 2010; Martin et al. 2020; Veras et al. 2020b), where the enhanced stellar luminosity will easily spin up 100 m — 10 km bodies within 7 au to their breaking point due to the YORP effect (Veras et al. 2014b; Veras & Scheeres 2020). Further, extant debris discs from main sequence evolution have been observed orbiting giant stars at distances of tens of au (Bonsor et al. 2013, 2014).

During the white dwarf phase, boulders, pebbles and dust are subject to radiative drag or Yarkovsky effects that gradually draw them into the star (Dong et al. 2010; Veras et al. 2015a,b, 2019a); upon approach these objects may fragment or sublimate before impacting the photosphere (Brown et al. 2017). Consequently, nearly all pollutant progenitors contribute to the formation and evolution of a white dwarf debris disc, of which over 40 have now been observed (Farihi 2016; Manser et al. 2020).

Gravitational instabilities amongst exo-planets can thrust exo-asteroids towards white dwarfs and instigate periods of bombardments³. Analogously, in the early stages of the solar system, the planetesimal disc was destabilised by the movements of the giant planets (Gomes et al. 2005). Lingering uncertainties about the timeline of the Late Heavy Bombardment even within our own solar system (Morbidelli et al. 2018; de Sousa Ribeiro et al. 2020) indicate that the details of similar events in post-main-sequence exo-systems are even more unconstrained.

However, the process of bombardment will nevertheless likely occur due to these instabilities. Projectiles will crash into both exo-asteroids and exo-planets, create craters, and eject material back into the interplanetary medium. This material in turn can be radiatively dragged towards the white dwarf or perturbed into it by the extant planetary system architecture. These processes can transport the chemical signature of the target surface to the white dwarf photosphere, where this signature may be measured.

1.2 Impact ejecta models

The mechanics of the impact ejecta process in white dwarf planetary systems has not previously been considered in detail. In contrast, impact ejecta has been the subject of extensive investigations within the solar system, as well as a few in other types of extrasolar planetary systems.

³ The influence of binary stellar companions in post-main-sequence planetary systems can also produce gravitational instabilities, sometimes through the Lidov-Kozai mechanism (Kratzer & Perets 2012; Veras & Tout 2012; Mustill et al. 2013; Portegies Zwart 2013; Bonsor & Veras 2015; Hamers & Portegies Zwart 2016; Kostov et al. 2016; Petrovich & Muñoz 2017; Stephan et al. 2017; Veras et al. 2017a,b; Stephan et al. 2018).

1.2.1 Previous studies

The physics of impact-induced mass loss from planetary bodies is best constrained from within the solar system. The origin of the lunar and martian meteorites has provided strong motivation for many investigations (e.g. Marcus 1969; O’Keefe & Ahrens 1977; Melosh 1984; Vickery & Melosh 1987; Head et al. 2002; Artemieva & Ivanov 2004; DeCarli et al. 2007; Artemieva & Shuvalov 2008; DeCarli 2013; Kurosawa et al. 2018). Lithopanspermia provides another motivation, both inside and outside of the solar system (Melosh 1988, 2003; Krijt et al. 2017; Lingam & Loeb 2017; Veras et al. 2018b).

In general, impacts onto target bodies occur obliquely, and the most probable impact angle of randomly incident impactors is 45 degrees (Shoemaker 1962). The amount of ejecta depends on impact angle, as does the structure of the resultant crater and the peak shock pressure contour profiles (Burchell & Mackay 1998; Pierazzo & Melosh 2000a; Grey et al. 2002; Schultz & Wrobel 2012; Takizawa & Katsuragi 2019). As for the amount of material ejected, some trends emerge: the ejecta speed decreases as the impact angle increases to 90°, which corresponds to a vertical impact (see e.g. Figs. 6-7 of Anderson et al. 2003). Artemieva & Ivanov (2004) found that the amount of escaping material is minimized for vertical or near-vertical impacts (see their Table 1).

In addition to depending on the impact angle, the amount of mass ejected can be partitioned into three stages depending on ejection timing, location, velocity and experienced shock pressure (e.g. Johnson et al. 2014; Kurosawa et al. 2018; Kurosawa & Takada 2019):

- (i) Jetting (Kieffer 1977; Melosh & Sonett 1986; Ang 1990; Vickery 1993; Sugita & Schultz 1999; Johnson et al. 2014, 2015; Kurosawa et al. 2015),
- (ii) Spallation (Melosh 1984, 1985a; Vickery & Melosh 1987; Polanskey & Ahrens 1990; Head et al. 2002; Artemieva & Ivanov 2004; DeCarli et al. 2007; DeCarli 2013), and
- (iii) Normal excavation (e.g. Maxwell 1977; Croft 1980; Housen et al. 1983; Melosh 1985b; Cintala et al. 1999; Anderson et al. 2004; Housen & Holsapple 2011; Tsujido et al. 2015; Kurosawa & Takada 2019).

Extensive published work about each of these stages provides an indication of the complexity of impact cratering.

1.2.2 Current study

This level of complexity far exceeds what could be reasonably applied in extrasolar planetary systems, where the amount of available data is very sparse compared to that in the solar system. Therefore, we need to make broad assumptions in order to quantify this idea of generating metal pollution from impact ejecta.

Our three main assumptions are:

- (i) We assume vertical impacts on a plane-parallel surface. As previously demonstrated (Anderson et al. 2003; Artemieva & Ivanov 2004), doing so provides a lower bound on the ejecta mass. This bound will usefully help future investigators assess the plausibility of white dwarf pollution arising from impact ejecta in particular systems.

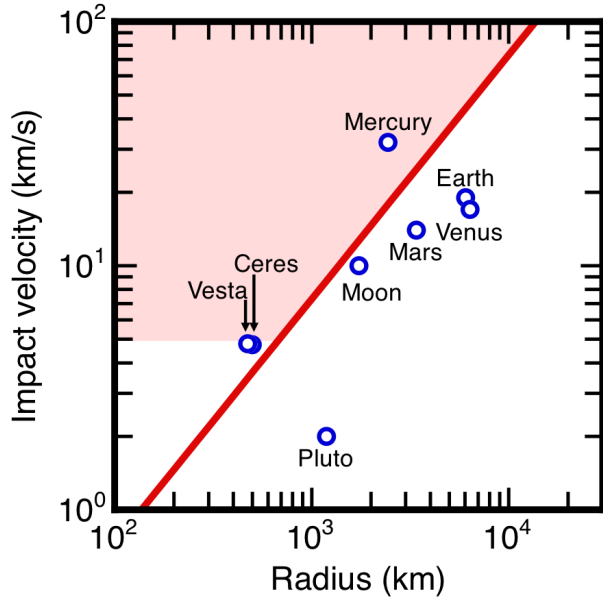


Figure 1. Required impact speed to satisfy the condition that the majority of the total ejecta mass arises from normal excavation. The radius on the x -axis is that of the target body (R_T). The blue circles show the mean impact speed on the bodies in the solar system (Ito & Malhotra 2006; O’Brien & Sykes 2011; Greenstreet et al. 2015). The red shaded regions indicate where the results of Kurosawa & Takada (2019) are applicable to the current study.

(ii) We adopt an analytical model, rather than perform laboratory experiments or run hydrodynamics codes. An analytical model will allow us to sample a large region of phase space that is relevant to white dwarf planetary systems, which would otherwise not be possible in a single paper with other methods. We use the full-chain analytical model from (Kurosawa & Takada 2019). The advantage of this model is that it allows for the high-speed cutoff of the ejecta in the regime of normal excavation to be estimated.

(iii) We neglect jetting and spallation. Unfortunately, neither simple analytical models for jetting and spallation nor tabular data under a wide range of impact conditions have been established, despite much progress and detailed laboratory and numerical impact experiments (e.g. Polansky & Ahrens 1990; Head et al. 2002; Artemieva & Ivanov 2004; Artemieva & Shuvalov 2008; Kurosawa et al. 2015, 2018). Hence, we assume that the large-scale mass ejection is dominated by normal excavation. Now we elaborate on this assumption.

In order to develop a criterion for mass ejecta being dominated by normal excavation, we first need to determine in what parameter regime normal excavation produces the greatest amount of ejecta mass. To do so, we need to establish the ejecta velocity distribution. Typically, this distribution is given by a power-law relation (Housen et al. 1983; Housen & Holsapple 2011).

Kurosawa & Takada (2019) provided an improvement by establishing a high-speed cutoff for this power-law. This upper limit was determined by the residual speed in the isobaric core, which — near the impact point — is estimated to be about 10 per cent of the impact speed. Thus, the ap-

plicable range of their results in a radius-impact velocity plane can be easily calculated as follows. The required impact speed $|\vec{v}_I|$ for the condition that the normal excavation is dominant in the total ejecta mass is given by

$$|\vec{v}_I| > \frac{v_{\text{esc}}}{\alpha} \quad (1)$$

where the escape speed from the target is

$$v_{\text{esc}} = \sqrt{\frac{2GM_T}{R_T}} = R_T \sqrt{\frac{8}{3} G \pi \rho_T}, \quad (2)$$

such that α is the ratio of the high-speed cutoff to the impact velocity, and M_T , R_T and ρ_T are the mass, radius and density of the target. Figure 1 illustrates $|\vec{v}_I|$ as a function of R_T . In this figure, we adopted $\alpha = 0.1$ and $\rho = 3000 \text{ kg/m}^3$. The mean impact speeds for planetary bodies in the solar system are also plotted for context.

The plot illustrates, as an example, that in our solar system, on average, asteroids in the main belt, as well as Mercury, would meet the condition. The red shaded region illustrates combinations of impact speed and target radii that are applicable in this paper, and will be used to inform the initial conditions of our simulations.

1.3 Plan for paper

In Sections 2 and 3, we respectively outline some additional assumptions and describe the model outputs. Then, in Section 4, we perform computations and summarise our results, primarily through a series of tables. We then address the observational constraints in Section 5, and provide two concrete examples of how this formalism may be used in Section 6. We discuss the results in Section 7, and conclude in Section 8. In order to aid the reader, we have listed descriptions of all of the variables used in this paper in Table 1.

2 ADDITIONAL MODEL ASSUMPTIONS

We now outline some additional model assumptions.

2.1 Impactor-to-target radii ratio

Our model relies on the plane-parallel geometry approximation, which is thought to be valid for a sufficiently small impactor relative to the size of the target. The approximation holds when $R_I/R_T \lesssim 0.2$, where R_I and R_T are respectively the radii of the impactor and target (Bierhaus et al. 2013; Marchi et al. 2014). We, however, take a more conservative approach: we perform computations only for systems where all of the mass which escapes the target is excavated within $0.2R_T$. Throughout the manuscript, variables or parameters with subscripts of I and T will refer to properties of the impactor and target respectively.

2.2 Atmosphere-less targets

We consider only atmosphere-less targets, ranging in size from 1 km up to 10^3 km (a Pluto-like object). These objects are typically not expected to have retained a primordial atmosphere at such a late stage of stellar evolution.

Over the course of a stellar lifetime, stars can

Table 1. Variables used in this paper.

Variable	Explanation	Reference
A	Auxiliary variable	Equation (12)
B	Auxiliary variable	Equation (13)
c_I	Bulk sound speed in the impactor	Table 2
c_T	Bulk sound speed in the target	Table 2
$C_{T,c}$	Dimensionless cold coefficient of the target	Table 2
$C_{T,h}$	Dimensionless thermal coefficient of the target	Table 2
d	Distance from the white dwarf at which collision occurs	Chosen by user
D	Horizontal distance along target surface to impact point	Chosen by user
ΔD	Streamtube width along target surface to impact point	Chosen by user
E_{gra}	Gravitational energy	Equation (9)
E_{kin}	Kinetic energy	Equation (15)
E_{max}	Maximum impact energy to survive target break-up	Equation (20)
F_I	Dimensionless coefficient for impactor	Table 2
F_T	Dimensionless coefficient for target	Table 2
g_T	Gravitational acceleration at surface of target	Equation (10)
K	Auxiliary variable	Equation (14)
l	Auxiliary variable	Equation (19)
$m_{T,c}$	Dimensionless cold exponent of target	Table 2
$m_{T,h}$	Dimensionless thermal exponent of target	Table 2
M_{exc}	Total mass of the excavated (not necessarily escaping) material	Equation (7)
M_I	Mass of the impactor	Chosen by user
M_{tube}	Mass in a streamtube	Equation (6)
M_T	Mass of the target	Chosen by user
n	Dimensionless shock decay exponent	Chosen by user
R_I	Radius of the impactor	Chosen by user
R_T	Radius of the target	Chosen by user
R_{WD}	Radius of the white dwarf	Chosen by user
$u_{T,sw}$	Switching speed of target	Table 2
$u_{T,th}$	Threshold speed of target	Table 2
$u_{T,0}$	The peak target material speed in an isobaric core	Equation (11)
\vec{v}_E	Ejecta velocity	Equation (8)
\vec{v}_I	Impact velocity	Chosen by user
v_{esc}	Escape speed from surface of target	Equation (2)
v_{orb}	Orbital speed of the target	Equation (3)
Z	Dimensionless streamline shape coefficient	Chosen by user
ϵ	Auxiliary variable	Equation (18)
θ	Impactor angle, assuming 0° is parallel to target surface	Chosen by user
ρ_T	Density of target	Table (2)
ϕ	Ejecta angle, assuming 0° is parallel to target surface	Equation (5)

strip away atmospheres of planets and moons which are within a critical distance of the star. This critical distance increases significantly during the giant branch phase of evolution⁴. Investigations which have considered this critical distance (Livio & Soker 1984; Goldstein 1987; Nelemans & Tauris 1998; Soker 1998; Villaver & Livio 2007; Wickramasinghe et al. 2010; Bear & Soker 2011; Schreiber et al. 2019) (see Section 6.1.2. of Veras 2016b for a summary) have not converged on a specific expression for

this value. The ability of a planet to retain a certain fraction of its atmosphere throughout stellar evolution remains an open question.

Regardless, one may reasonably assume based on the above studies that rocky bodies which have survived the giant branch phases of stellar evolution intact within tens of au of their parent stars have lost their atmospheres.

2.3 Impact speed range

Our choice of impact speed $|\vec{v}_I|$, which is a relative speed between the impactor and target, is dictated by equation (1). This speed is weakly dependent on d , the distance from

⁴ This radiation also changes the chemical composition of the portions of atmospheres which survive (Campbell et al. 1988; Spiegel & Madhusudhan 2012).

Table 2. Physical parameters for four different types of materials.

Property	Granite	Basalt	Water (at 25°C)	Iron
c (km/s)	3.68	2.6	2.393	3.80
$C_{T,c}$	0.0412	0.0281	0.0796	0.0235
$C_{T,h}$	0.0833	0.0827	0.145	0.0691
$m_{T,c}$	1.97	2.29	1.39	2.14
$m_{T,h}$	1.20	1.21	1.04	1.25
F	1.24	1.62	1.333	1.58
$u_{T,th}$ (km/s)	0.804	0.730	1.48	0.652
$u_{T,sw}$ (km/s)	2.12	2.67	5.03	3.19
ρ (kg/m ³)	2630	2860	998	7680

the white dwarf to the collision site. Although increasing d likely helps to decrease $|\vec{v}_I|$, there is no direct correlation without specification of the geometry of the collision and the geometry of the orbit. Hence, d does not represent an input into our simulations.

Instead the range of $|\vec{v}_I|$ that we provide spans most realistic values. The lowest value is 5 km/s, which is the lower limit at which the full-chain model from Kurosawa & Takada (2019) is applicable. For an upper bound, Eq. 7 of Veras et al. (2014c) illustrates that an impactor could reach speeds relative to the white dwarf of up to 1000 km/s.⁵ Our formalism is not applicable for such high-velocity impacts, but can model collisions with impact speeds reaching 100 km/s.

That value of 100 km/s is still relatively high for white dwarf planetary systems. For example, the maximum speed of any orbit occurs at its orbital pericentre, where (as derived by assuming an orbital eccentricity of unity and neglecting the mass of the target)

$$\begin{aligned} \max(v_{\text{orb}}) &\approx \sqrt{\frac{2GM_{\text{WD}}}{d}} \\ &= 14.6 \frac{\text{km}}{\text{s}} \left(\frac{M_{\text{WD}}}{0.6M_{\odot}}\right)^{1/2} \left(\frac{d}{5 \text{ au}}\right)^{-1/2}. \end{aligned} \quad (3)$$

By providing values for $|\vec{v}_I|$, rather than making any assumptions about elliptic orbits, we also allow for the possibility for a collision to occur between one or two bodies on parabolic or hyperbolic orbits⁶.

2.4 Neglecting vaporized mass

Impactors can melt and vaporize some of the mass which would otherwise escape the target. The amount of vaporized mass is a function of both the impact speed and angle. As demonstrated in Pierazzo & Melosh (2000b), the volume of vaporized mass increases with impact angle, peaking at 90°. Other experiments have established scaling laws as a function of this angle (Schultz 1996), also peaking at 90°.

⁵ The reason is because exo-asteroids have to pass inside the Roche radius of the white dwarf in order to eventually pollute it, and the Roche radius for a typical rubble pile is located at a distance of about 0.005 au (Veras et al. 2017b).

⁶ One or both bodies could be heading out of the system on a hyperbolic orbit following a gravitational instability.

As suggested by Pierazzo et al. (1997), vaporization does not become important until $|\vec{v}_I| \gtrsim 50$ km/s, and only for material which lies within a couple of R_I of the impact point. Therefore, if most of the would-be-ejected material is close to the impact point, then vaporization would significantly affect our high-impact speed computations.

In fact, the reality is otherwise: as we will show, the amount of ejecta mass which escapes the target increases with distance from the impact point, usually for distances of at least tens of R_I . Hence, the fraction of escaped mass which would have been vaporized by the impact is typically negligible. Regardless, in order to be conservative, we report simulation results only for impact events where mass escapes out to a horizontal distance of at least $15R_I$.

Also, a key consideration in cratering mechanics is the dissipation of the expanding shock wave that is produced by the impact. The pressure decay of this wave is parametrized by a dimensionless exponent n that will appear in many of the subsequent equations. Rather than use a constant value for n , we instead adopt the following, more realistic speed-dependent exponent from Pierazzo et al. (1997) in our computations:

$$n = -1.84 + 2.61 \log \left(\left| \frac{v_I}{\text{km/s}} \right| \right). \quad (4)$$

Further, Pierazzo et al. (1997) reported that the numerical values in equation (4) are relatively insensitive to the target material.

3 MODEL OUTPUTS

Now we discuss in detail some of the properties of the full-chain analytical model from Kurosawa & Takada (2019) that we adopt here.

3.1 Ejecta direction

As in Kurosawa & Takada (2019), we utilise the Maxwell Z -model. This model represents a way to analytically characterize streamlines in cratering physics, and was borne out of empirical relations noticed in experiments performed by the United States Defense Nuclear Agency (Maxwell 1977). The value of Z is mapped to a streamline containing ejecta which is thrust outward at an angle of

$$\phi = \tan^{-1}(Z - 2). \quad (5)$$

Here $\phi = 0^\circ$ corresponds to the target surface, and Z ranges from 2-5 ($\phi = 0.0^\circ - 71.6^\circ$) because that range is consistent with values measured in laboratory experiments (Cintala et al. 1999; Yamamoto et al. 2017). Further, $Z = 3$ is adopted for illustration purposes because it yields the ejection angle of 45 degrees, a typical value observed in these laboratory experiments. Note that the angle ϕ is independent of D , the distance along the (assumed flat) target surface to the impact point.

3.2 Ejecta mass

The mass in a specific streamtube M_{tube} between the distances $(D - \Delta D)$ and D is given by

$$M_{\text{tube}}(D - \Delta D; D) = 2\pi \left(\frac{Z - 2}{Z + 1} \right) \rho_T D^2 \Delta D, \quad (6)$$

where ρ_T is the density of target and ΔD is the streamtube width along the surface. This interval notation will be used throughout the manuscript for clarity.

Any melted mass will be solidified rapidly after the pressure release, and we neglect vaporized mass as explained above. The cumulative mass excavated from the surface due to a single impact can then be expressed as M_{exc} , where, for a fixed ΔD ,

$$M_{\text{exc}} = \sum_{D=\Delta D} [M_{\text{tube}}(D - \Delta D; D)]. \quad (7)$$

Determining the fraction of M_{exc} which actually escapes the target is a main goal of the paper, and depends on the ejecta speed. For a numerical implementation of equation (7), we set the upper bound of the summation to $0.2R_T$ (see Section 2.1). One can choose the value of ΔD depending on the accuracy of the final result which is sought; different values of ΔD can be easily implemented given the computational speed of the analytical model.

3.3 Ejecta velocity

The ejecta velocity (\vec{v}_E) includes direction through the angle ϕ given by equation (5) and magnitude through Eq. (20) of Kurosawa & Takada (2019). They provide this magnitude within a streamtube in terms of the kinetic and gravitational energies ($E_{\text{kin}}, E_{\text{gra}}$)⁷ within that same streamtube as

$$|\vec{v}_E(D - \Delta D; D)| = \sqrt{\frac{2[E_{\text{kin}}(D - \Delta D; D) - E_{\text{gra}}(D - \Delta D; D)]}{M_{\text{tube}}(D - \Delta D; D)}}. \quad (8)$$

These individual energies are given by Eqs. (27-36) of Kurosawa & Takada (2019), and each include the arbitrary lengthscale ΔD which cancels out in the computation of $|\vec{v}_E(D - \Delta D; D)|$ for a particular streamtube. Therefore, $|\vec{v}_E(D - \Delta D; D)|$ is independent of ΔD , but is dependent on D , and tends towards 0 as D increases.

The gravitational energy

⁷ They also incorporate strength energy, but have caveats about its applicability within the model. We henceforth neglect the internal strength of our targets.

$$E_{\text{gra}}(D - \Delta D; D) = \pi \left[\frac{Z^2 - 4Z + 4}{Z(Z + 2)} \right] g_T \rho_T D^3 \Delta D \quad (9)$$

is a function of the density ρ_T and surface gravity g_T of the target, the latter of which is given by

$$g_T = \frac{GM_T}{R_T^2}, \quad (10)$$

with M_T representing the mass of the target. Further, all targets are assumed to be spheres. This assumption allows one to easily compute the target mass (M_T) given ρ_T and R_T .

The kinetic energy (E_{kin}) contains several terms, and these in turn include several dimensionless constants and speeds. They all refer to properties of the target ($m_{T,c}, m_{T,h}, C_{T,c}, C_{T,h}$), where the subscripts ‘‘c’’ and ‘‘h’’ refer to ‘‘cold’’ and ‘‘hot’’. Two of the speeds ($u_{T,sw}, u_{T,th}$: ‘‘switching’’ and ‘‘threshold’’) also refer to properties of the target material. All these values are given for a variety of materials (granite, basalt, water and iron) in Table 2 and described in physical detail in Kurosawa & Takada (2019).

One important speed is $u_{T,0}$, which is the peak target material speed in an isobaric core. This speed is dependent on several variables, including the impact speed $|\vec{v}_I|$ (technically, the speed of the impactor at the target surface). The value of $u_{T,0}$ is computed by using the formulation on Pg. 231 of Melosh (2011) (originally from Melosh 1989), which illustrates

$$u_{T,0} = \frac{-B + \sqrt{B^2 - 4AK}}{2A}, \quad \text{if } A \neq 0$$

$$= \frac{|\vec{v}_I|}{2}, \quad \text{if } A = 0 \quad (11)$$

where

$$A \equiv \rho_T F_T - \rho_I F_I, \quad (12)$$

$$B \equiv \rho_T c_T + \rho_I c_I + 2\rho_I F_I |\vec{v}_I|, \quad (13)$$

$$K \equiv -\rho_I |\vec{v}_I| (c_I + F_I |\vec{v}_I|). \quad (14)$$

The values c_T, c_I , and F_I represent more parameters specific to the target and the impactor, and are given in Table 2 (reproduced from Melosh 2011). Note that for equal-composition impactors and targets, $A = 0$.

The kinetic energy is either, for $u_{T,0} > u_{T,sw}$,

$$E_{\text{kin}}(D - \Delta D; D) = R_I^{Z+1} D^{1-Z} \Delta D \left\{ \pi \left[\frac{Z - 2}{Z + 1} \right] \rho_T C_{T,h}^2 u_{T,0}^{2m_{T,h}} \right.$$

$$+ \left[\frac{\pi(Z - 2) \rho_T C_{T,h}^2}{2nm_{T,h} - Z - 1} \right] \left(u_{T,0}^{2m_{T,h}} + u_{T,0}^{\frac{Z+1}{n}} u_{T,sw}^{\frac{2nm_{T,h} - Z - 1}{n}} \right)$$

$$\left. + \left[\frac{\pi(Z - 2) \rho_T C_{T,c}^2}{2nm_{T,c} - Z - 1} \right] \left(u_{T,sw}^{\frac{2nm_{T,c} - Z - 1}{n}} - u_{T,th}^{\frac{2nm_{T,c} - Z - 1}{n}} \right) u_{T,0}^{\frac{Z+1}{n}} \right\}, \quad (15)$$

or, for $u_{T,0} < u_{T,sw}$,

$$E_{\text{kin}}(D - \Delta D; D) = \pi R_I^{Z+1} D^{1-Z} \Delta D \rho_T C_{T,c}^2 \left\{ \left[\frac{Z - 2}{Z + 1} \right] u_{T,0}^{2m_{T,c}} \right.$$

$$\left. + \left[\frac{Z - 2}{2nm_{T,c} - Z - 1} \right] \left(u_{T,0}^{2m_{T,c}} + u_{T,0}^{\frac{Z+1}{n}} u_{T,th}^{\frac{2nm_{T,c} - Z - 1}{n}} \right) \right\}.$$

(16)

3.4 Escaping the target

Excavated material will escape the gravitational pull of the target only when $|\vec{v}_E| > v_{\text{esc}}$. Because $|\vec{v}_E|$ is a function of D , there will be a critical value of D beyond which escape is not possible, where the ejecta will re-impact the target. Computing this critical value of D allows us to determine the cumulative escaped mass from all inward streamtubes. If mass does escape the target, then it will escape with an “excess speed” equal to $\sqrt{|\vec{v}_E|^2 - v_{\text{esc}}^2}$ for a given streamline.

4 SIMULATION INPUTS AND RESULTS

By using the formalism of the last section, we can compute the amount of mass ejected due to a single impact. Doing so first involves solving equation (8) for each streamtube. We set $\Delta D = 10^{-4} \times (0.2R_T)$ uniformly across all simulations, which achieves a balance of accuracy and speed across the wide range of parameter space studied. We emphasise that in order to obtain a higher accuracy for any particular setup, the computation should be rerun with progressively smaller ΔD until the desired result is acquired.

4.1 Input variables

Only in rare cases will the direction of the escaped material be towards the white dwarf, which represents an Earth-sized target. Instead, the ejected matter will populate reservoirs of debris that may themselves be perturbed at a later time towards the white dwarf, or slowly dragged into the white dwarf due to Poynting-Robertson drag. Hence, when modelling debris trajectories – and keeping in mind that vertical impacts yield a lower bound for the amount of escaped mass – one must couple the escape direction with the orbital architecture, the geometry of the collision, and the excess speed. We consider escaped mass values across the entire range $Z = 2.01 - 5$ at seven values, thereby avoiding the singularities which occur at $Z = 2$.

A final consideration is the potential destruction of the target due to the impact. The full-chain analytical model applies only when initial conditions are chosen so that the impactor does not destroy the target during the collision. Section 5 of Movshovitz et al. (2016) provided a concise analytical formulation for when the target would break apart due to an impactor:

$$\left(\frac{1}{2}\right) \left(\frac{\epsilon M_T + M_I}{M_T + M_I}\right) \left(\frac{M_T M_I}{M_T + M_I}\right) |\vec{v}_I|^2 > E_{\text{max}} \quad (17)$$

where

$$\epsilon \equiv \begin{cases} \frac{3R_I l^2 - l^3}{4R_I^3}, & l < 2R_I \\ 1, & l \geq 2R_I \end{cases}, \quad (18)$$

$$l \equiv (R_T + R_I)(1 - \cos \theta), \quad (19)$$

and

$$E_{\text{max}} = (13.4 \pm 10.8) \left[\frac{3GM_T^2}{5R_T} + \frac{3GM_I^2}{5R_I} + \frac{GM_T M_I}{R_T + R_I} \right], \quad (20)$$

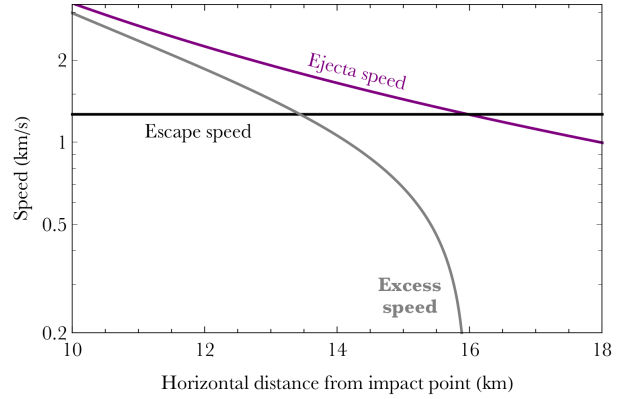


Figure 2. Detail of how the post-collision ejecta speed tapers off as a function of distance from the impact point, eventually falling below the escape speed of the target body. The excess speed is the ejecta’s speed upon leaving the gravitational pull of the target. These quantities were computed for $R_T = 10^3$ km, $R_I = 10^{-4}R_T$, $|\vec{v}_I| = 10$ km/s, $Z = 3$ and basaltic impactors and targets.

where the numerical range given is conservative and encompasses $\theta = 45^\circ - 90^\circ$. The relations in equations (17-20) can be reduced to just two degrees of freedom if a head-on collision of equal-composition impactor and target are assumed (see Eq. 21 of Veras et al. 2018b). For a basaltic impactor and target, here we approximate the destruction condition in that equation as

$$\frac{|\vec{v}_I|}{v_{\text{esc}}} \gtrsim \sqrt{3 \left(\frac{R_T}{R_I}\right)^3} \quad (21)$$

and use equation (21) to determine when a target would be destroyed.

4.2 Simulation data

We present our main results in the form of four data tables (Tables 3-6) and some supplementary plots of specific cases (Figs. 2-6). Tables 3-5 display results for a basaltic impactor and target, where, respectively, $R_I = 10^{-5}, 10^{-4}, 10^{-3}R_T$.

In all tables, the escaped mass is given in terms of M_I to two significant figures. This presentation (i) enables one to quickly scan the phase space to see where there is a guaranteed increase of mass in interplanetary space due to a collision (when the value is greater than unity, which is nearly everywhere), (ii) keeps the magnitude of the numbers tractable, and (iii) and reflects the approximate nature of these results, which is appropriate given the current constraints in white dwarf planetary systems.

Non-numeric table entries reveal other aspects of these collisions. A value of “APART” indicates likely destruction of the target based on equation (21). Values of “LIMIT” indicate that the full-chain analytical model cannot approximate the escaped mass well enough to be used here, based on mass escaping at our limiting location of $D = 0.2R_T$. “JET” indicates that equation (1) is not satisfied (such that jetting and spallation might dominate mass escape), and “VAPOR” indicates that the value of D within which mass escape ceases is under $15R_I$ (indicating a potential, but still likely low, contribution from vaporized mass).

The presentation of Tables 3-5 reflects the strongest de-

Table 3. Mass which escapes into the interplanetary medium after a collision between a spherical basaltic impactor and a spherical basaltic target, where $R_I = 10^{-5}R_T$, for given target radii, impact speeds, and the entire range of Z (streamtube shape) values. Results are given in both kg and (immediately below in parenthesis) the impactor mass M_I . “APART” refers to cases where the target would be destroyed, “LIMIT” where the plane-parallel approximation of the full-chain analytical model breaks down, “JET” where the impact speed fails to satisfy equation (1), and “VAPOR” for where the amount of vaporized mass may not be negligible. See the main text for more details.

Cumulative escaped mass in terms of both kg and M_I							
$R_I = 10^{-5}R_T$	$Z = 2.01$	$Z = 2.5$	$Z = 3.0$	$Z = 3.5$	$Z = 4.0$	$Z = 4.5$	$Z = 5.0$
$R_T = 1 \text{ km}$							
$ \vec{v}_I = 5 \text{ km/s}$	$3.2 \times 10^7 \text{ kg}$ ($2.7 \times 10^9 M_I$)	$2.8 \times 10^7 \text{ kg}$ ($2.3 \times 10^9 M_I$)	$2.3 \times 10^6 \text{ kg}$ ($1.9 \times 10^8 M_I$)	$3.0 \times 10^5 \text{ kg}$ ($2.5 \times 10^7 M_I$)	$5.4 \times 10^4 \text{ kg}$ ($4.5 \times 10^6 M_I$)	$1.3 \times 10^4 \text{ kg}$ ($1.1 \times 10^6 M_I$)	$4.1 \times 10^3 \text{ kg}$ ($3.4 \times 10^5 M_I$)
$ \vec{v}_I = 10 \text{ km/s}$	LIMIT	$1.8 \times 10^9 \text{ kg}$ ($1.5 \times 10^{11} M_I$)	$1.9 \times 10^8 \text{ kg}$ ($1.6 \times 10^{10} M_I$)	$3.0 \times 10^7 \text{ kg}$ ($2.5 \times 10^9 M_I$)	$6.6 \times 10^6 \text{ kg}$ ($5.5 \times 10^8 M_I$)	$1.9 \times 10^6 \text{ kg}$ ($1.6 \times 10^8 M_I$)	$6.7 \times 10^5 \text{ kg}$ ($5.6 \times 10^7 M_I$)
$ \vec{v}_I = 30 \text{ km/s}$	LIMIT	$3.0 \times 10^8 \text{ kg}$ ($2.5 \times 10^{10} M_I$)	$3.0 \times 10^7 \text{ kg}$ ($2.5 \times 10^9 M_I$)	$4.4 \times 10^6 \text{ kg}$ ($3.7 \times 10^8 M_I$)	$9.0 \times 10^5 \text{ kg}$ ($7.5 \times 10^7 M_I$)	$2.4 \times 10^5 \text{ kg}$ ($2.0 \times 10^7 M_I$)	$7.9 \times 10^4 \text{ kg}$ ($6.6 \times 10^6 M_I$)
$ \vec{v}_I = 60 \text{ km/s}$	LIMIT	$2.0 \times 10^8 \text{ kg}$ ($1.7 \times 10^{10} M_I$)	$2.2 \times 10^7 \text{ kg}$ ($1.8 \times 10^9 M_I$)	$3.1 \times 10^6 \text{ kg}$ ($2.6 \times 10^8 M_I$)	$6.5 \times 10^5 \text{ kg}$ ($5.4 \times 10^7 M_I$)	$1.7 \times 10^5 \text{ kg}$ ($1.4 \times 10^7 M_I$)	$5.8 \times 10^4 \text{ kg}$ ($4.8 \times 10^6 M_I$)
$ \vec{v}_I = 100 \text{ km/s}$	$1.4 \times 10^8 \text{ kg}$ ($1.2 \times 10^{10} M_I$)	$1.7 \times 10^8 \text{ kg}$ ($1.4 \times 10^{10} M_I$)	$1.8 \times 10^7 \text{ kg}$ ($1.5 \times 10^9 M_I$)	$2.6 \times 10^6 \text{ kg}$ ($2.2 \times 10^8 M_I$)	$5.5 \times 10^5 \text{ kg}$ ($4.6 \times 10^7 M_I$)	$1.4 \times 10^5 \text{ kg}$ ($1.2 \times 10^7 M_I$)	$5.0 \times 10^4 \text{ kg}$ ($4.2 \times 10^6 M_I$)
$R_T = 10 \text{ km}$							
$ \vec{v}_I = 5 \text{ km/s}$	$3.4 \times 10^8 \text{ kg}$ ($2.8 \times 10^7 M_I$)	$5.3 \times 10^8 \text{ kg}$ ($4.4 \times 10^7 M_I$)	$7.4 \times 10^7 \text{ kg}$ ($6.2 \times 10^6 M_I$)	$1.4 \times 10^7 \text{ kg}$ ($1.2 \times 10^6 M_I$)	$3.5 \times 10^6 \text{ kg}$ ($2.9 \times 10^5 M_I$)	$1.1 \times 10^6 \text{ kg}$ ($8.9 \times 10^4 M_I$)	$4.0 \times 10^5 \text{ kg}$ ($3.3 \times 10^4 M_I$)
$ \vec{v}_I = 10 \text{ km/s}$	$1.8 \times 10^{10} \text{ kg}$ ($1.5 \times 10^9 M_I$)	$3.5 \times 10^{10} \text{ kg}$ ($2.9 \times 10^9 M_I$)	$6.1 \times 10^9 \text{ kg}$ ($5.1 \times 10^8 M_I$)	$1.4 \times 10^9 \text{ kg}$ ($1.2 \times 10^8 M_I$)	$4.2 \times 10^8 \text{ kg}$ ($3.5 \times 10^7 M_I$)	$1.6 \times 10^8 \text{ kg}$ ($1.3 \times 10^7 M_I$)	$6.6 \times 10^7 \text{ kg}$ ($5.5 \times 10^6 M_I$)
$ \vec{v}_I = 30 \text{ km/s}$	$2.8 \times 10^9 \text{ kg}$ ($2.3 \times 10^8 M_I$)	$5.8 \times 10^9 \text{ kg}$ ($4.8 \times 10^8 M_I$)	$9.6 \times 10^8 \text{ kg}$ ($8.0 \times 10^7 M_I$)	$2.0 \times 10^8 \text{ kg}$ ($1.7 \times 10^7 M_I$)	$5.6 \times 10^7 \text{ kg}$ ($4.7 \times 10^6 M_I$)	$1.9 \times 10^7 \text{ kg}$ ($1.6 \times 10^6 M_I$)	$7.7 \times 10^6 \text{ kg}$ ($6.4 \times 10^5 M_I$)
$ \vec{v}_I = 60 \text{ km/s}$	$1.8 \times 10^9 \text{ kg}$ ($1.5 \times 10^8 M_I$)	$3.8 \times 10^9 \text{ kg}$ ($3.2 \times 10^8 M_I$)	$6.7 \times 10^8 \text{ kg}$ ($5.6 \times 10^7 M_I$)	$1.4 \times 10^8 \text{ kg}$ ($1.2 \times 10^7 M_I$)	$4.1 \times 10^7 \text{ kg}$ ($3.4 \times 10^6 M_I$)	$1.4 \times 10^7 \text{ kg}$ ($1.2 \times 10^6 M_I$)	$5.9 \times 10^6 \text{ kg}$ ($4.9 \times 10^5 M_I$)
$ \vec{v}_I = 100 \text{ km/s}$	$1.4 \times 10^9 \text{ kg}$ ($1.2 \times 10^8 M_I$)	$3.2 \times 10^9 \text{ kg}$ ($2.7 \times 10^8 M_I$)	$5.5 \times 10^8 \text{ kg}$ ($4.6 \times 10^7 M_I$)	$1.2 \times 10^8 \text{ kg}$ ($1.0 \times 10^7 M_I$)	$3.5 \times 10^7 \text{ kg}$ ($2.9 \times 10^6 M_I$)	$1.2 \times 10^7 \text{ kg}$ ($1.0 \times 10^6 M_I$)	$5.0 \times 10^6 \text{ kg}$ ($4.2 \times 10^5 M_I$)
$R_T = 100 \text{ km}$							
$ \vec{v}_I = 5 \text{ km/s}$	$3.4 \times 10^9 \text{ kg}$ ($2.8 \times 10^5 M_I$)	$1.0 \times 10^{10} \text{ kg}$ ($8.6 \times 10^5 M_I$)	$2.3 \times 10^9 \text{ kg}$ ($1.9 \times 10^5 M_I$)	$6.5 \times 10^8 \text{ kg}$ ($5.4 \times 10^4 M_I$)	$2.2 \times 10^8 \text{ kg}$ ($1.8 \times 10^4 M_I$)	$8.1 \times 10^7 \text{ kg}$ ($6800 M_I$)	$3.6 \times 10^7 \text{ kg}$ ($3000 M_I$)
$ \vec{v}_I = 10 \text{ km/s}$	$1.8 \times 10^{11} \text{ kg}$ ($1.5 \times 10^7 M_I$)	$6.8 \times 10^{11} \text{ kg}$ ($5.7 \times 10^7 M_I$)	$1.9 \times 10^{11} \text{ kg}$ ($1.6 \times 10^7 M_I$)	$6.5 \times 10^{10} \text{ kg}$ ($5.4 \times 10^6 M_I$)	$2.6 \times 10^{10} \text{ kg}$ ($2.2 \times 10^6 M_I$)	$1.2 \times 10^{10} \text{ kg}$ ($1.0 \times 10^6 M_I$)	$6.7 \times 10^9 \text{ kg}$ ($5.6 \times 10^5 M_I$)
$ \vec{v}_I = 30 \text{ km/s}$	$2.8 \times 10^{10} \text{ kg}$ ($2.3 \times 10^6 M_I$)	$1.1 \times 10^{11} \text{ kg}$ ($9.2 \times 10^6 M_I$)	$3.0 \times 10^{10} \text{ kg}$ ($2.5 \times 10^6 M_I$)	$9.6 \times 10^9 \text{ kg}$ ($8.0 \times 10^5 M_I$)	$3.6 \times 10^9 \text{ kg}$ ($3.0 \times 10^5 M_I$)	$1.6 \times 10^9 \text{ kg}$ ($1.3 \times 10^5 M_I$)	$7.4 \times 10^8 \text{ kg}$ ($6.2 \times 10^4 M_I$)
$ \vec{v}_I = 60 \text{ km/s}$	$1.8 \times 10^{10} \text{ kg}$ ($1.5 \times 10^6 M_I$)	$7.5 \times 10^{10} \text{ kg}$ ($6.3 \times 10^6 M_I$)	$2.2 \times 10^{10} \text{ kg}$ ($1.8 \times 10^6 M_I$)	$6.8 \times 10^9 \text{ kg}$ ($5.7 \times 10^5 M_I$)	$2.6 \times 10^9 \text{ kg}$ ($2.2 \times 10^5 M_I$)	$1.2 \times 10^9 \text{ kg}$ ($9.6 \times 10^4 M_I$)	$5.5 \times 10^8 \text{ kg}$ ($4.6 \times 10^4 M_I$)
$ \vec{v}_I = 100 \text{ km/s}$	$1.4 \times 10^{10} \text{ kg}$ ($1.2 \times 10^6 M_I$)	$6.1 \times 10^{10} \text{ kg}$ ($5.1 \times 10^6 M_I$)	$1.8 \times 10^{10} \text{ kg}$ ($1.5 \times 10^6 M_I$)	$5.9 \times 10^9 \text{ kg}$ ($4.9 \times 10^5 M_I$)	$2.2 \times 10^9 \text{ kg}$ ($1.8 \times 10^5 M_I$)	$9.7 \times 10^8 \text{ kg}$ ($8.1 \times 10^4 M_I$)	$5.0 \times 10^8 \text{ kg}$ ($4.2 \times 10^4 M_I$)
$R_T = 10^3 \text{ km}$							
$ \vec{v}_I = 5 \text{ km/s}$	JET						
$ \vec{v}_I = 10 \text{ km/s}$	$1.8 \times 10^{12} \text{ kg}$ ($1.5 \times 10^5 M_I$)	$1.3 \times 10^{13} \text{ kg}$ ($1.1 \times 10^6 M_I$)	$6.0 \times 10^{12} \text{ kg}$ ($5.0 \times 10^5 M_I$)	$3.0 \times 10^{12} \text{ kg}$ ($2.5 \times 10^5 M_I$)	$1.7 \times 10^{12} \text{ kg}$ ($1.4 \times 10^5 M_I$)	$9.7 \times 10^{11} \text{ kg}$ ($8.1 \times 10^4 M_I$)	$6.8 \times 10^{11} \text{ kg}$ ($5.7 \times 10^4 M_I$)
$ \vec{v}_I = 30 \text{ km/s}$	$2.8 \times 10^{11} \text{ kg}$ ($2.3 \times 10^4 M_I$)	$2.2 \times 10^{12} \text{ kg}$ ($1.8 \times 10^5 M_I$)	$9.8 \times 10^{11} \text{ kg}$ ($8.2 \times 10^4 M_I$)	$4.6 \times 10^{11} \text{ kg}$ ($3.8 \times 10^4 M_I$)	$2.2 \times 10^{11} \text{ kg}$ ($1.8 \times 10^4 M_I$)	$1.4 \times 10^{11} \text{ kg}$ ($1.2 \times 10^4 M_I$)	$7.3 \times 10^{10} \text{ kg}$ ($6100 M_I$)
$ \vec{v}_I = 60 \text{ km/s}$	$1.9 \times 10^{11} \text{ kg}$ ($1.6 \times 10^4 M_I$)	$1.4 \times 10^{12} \text{ kg}$ ($1.2 \times 10^5 M_I$)	$6.8 \times 10^{11} \text{ kg}$ ($5.7 \times 10^4 M_I$)	$3.4 \times 10^{11} \text{ kg}$ ($2.8 \times 10^4 M_I$)	$1.7 \times 10^{11} \text{ kg}$ ($1.4 \times 10^4 M_I$)	$9.8 \times 10^{10} \text{ kg}$ ($8200 M_I$)	$5.9 \times 10^{10} \text{ kg}$ ($4900 M_I$)
$ \vec{v}_I = 100 \text{ km/s}$	$1.4 \times 10^{11} \text{ kg}$ ($1.2 \times 10^4 M_I$)	$1.2 \times 10^{12} \text{ kg}$ ($9.8 \times 10^4 M_I$)	$5.9 \times 10^{11} \text{ kg}$ ($4.9 \times 10^4 M_I$)	$2.6 \times 10^{11} \text{ kg}$ ($2.2 \times 10^4 M_I$)	$1.4 \times 10^{11} \text{ kg}$ ($1.2 \times 10^4 M_I$)	$8.1 \times 10^{10} \text{ kg}$ ($6800 M_I$)	$4.7 \times 10^{10} \text{ kg}$ ($3900 M_I$)

Table 4. Same as Table 3, but for $R_I = 10^{-4}R_T$.

Cumulative escaped mass in terms of both kg and M_I							
$R_I = 10^{-4}R_T$	$Z = 2.01$	$Z = 2.5$	$Z = 3.0$	$Z = 3.5$	$Z = 4.0$	$Z = 4.5$	$Z = 5.0$
$R_T = 1 \text{ km}$							
$ \vec{v}_I = 5 \text{ km/s}$	LIMIT	LIMIT	$2.3 \times 10^9 \text{ kg}$	$3.0 \times 10^8 \text{ kg}$	$5.4 \times 10^7 \text{ kg}$	$1.3 \times 10^7 \text{ kg}$	$4.1 \times 10^6 \text{ kg}$
	LIMIT	LIMIT	$(1.9 \times 10^8 M_I)$	$(2.5 \times 10^7 M_I)$	$(4.5 \times 10^6 M_I)$	$(1.1 \times 10^6 M_I)$	$(3.4 \times 10^5 M_I)$
$ \vec{v}_I = 10 \text{ km/s}$	LIMIT	LIMIT	LIMIT	LIMIT	$6.5 \times 10^9 \text{ kg}$	$1.9 \times 10^9 \text{ kg}$	$6.6 \times 10^8 \text{ kg}$
	LIMIT	LIMIT	LIMIT	LIMIT	$(5.4 \times 10^8 M_I)$	$(1.6 \times 10^8 M_I)$	$(5.5 \times 10^7 M_I)$
$ \vec{v}_I = 30 \text{ km/s}$	LIMIT	LIMIT	LIMIT	$4.3 \times 10^9 \text{ kg}$	$8.9 \times 10^8 \text{ kg}$	$2.4 \times 10^8 \text{ kg}$	$7.8 \times 10^7 \text{ kg}$
	LIMIT	LIMIT	LIMIT	$(3.6 \times 10^8 M_I)$	$(7.4 \times 10^7 M_I)$	$(2.0 \times 10^7 M_I)$	$(6.5 \times 10^6 M_I)$
$ \vec{v}_I = 60 \text{ km/s}$	LIMIT	LIMIT	LIMIT	$3.1 \times 10^9 \text{ kg}$	$6.5 \times 10^8 \text{ kg}$	$1.7 \times 10^8 \text{ kg}$	$5.8 \times 10^7 \text{ kg}$
	LIMIT	LIMIT	LIMIT	$(2.6 \times 10^8 M_I)$	$(5.4 \times 10^7 M_I)$	$(1.4 \times 10^7 M_I)$	$(4.8 \times 10^6 M_I)$
$ \vec{v}_I = 100 \text{ km/s}$	LIMIT	LIMIT	LIMIT	$2.6 \times 10^9 \text{ kg}$	$5.5 \times 10^8 \text{ kg}$	$1.4 \times 10^8 \text{ kg}$	$4.9 \times 10^7 \text{ kg}$
	LIMIT	LIMIT	LIMIT	$(2.2 \times 10^8 M_I)$	$(4.6 \times 10^7 M_I)$	$(1.2 \times 10^7 M_I)$	$(4.1 \times 10^6 M_I)$
$R_T = 10 \text{ km}$							
$ \vec{v}_I = 5 \text{ km/s}$	LIMIT	$5.3 \times 10^{11} \text{ kg}$	$7.3 \times 10^{10} \text{ kg}$	$1.3 \times 10^{10} \text{ kg}$	$3.4 \times 10^9 \text{ kg}$	$1.1 \times 10^9 \text{ kg}$	$4.0 \times 10^8 \text{ kg}$
	LIMIT	$(4.4 \times 10^7 M_I)$	$(6.1 \times 10^6 M_I)$	$(1.1 \times 10^6 M_I)$	$(2.8 \times 10^5 M_I)$	$(9.0 \times 10^4 M_I)$	$(3.3 \times 10^4 M_I)$
$ \vec{v}_I = 10 \text{ km/s}$	LIMIT	LIMIT	$6.0 \times 10^{12} \text{ kg}$	$1.3 \times 10^{12} \text{ kg}$	$4.1 \times 10^{11} \text{ kg}$	$1.6 \times 10^{11} \text{ kg}$	$6.7 \times 10^{10} \text{ kg}$
	LIMIT	LIMIT	$(5.0 \times 10^8 M_I)$	$(1.1 \times 10^8 M_I)$	$(3.4 \times 10^7 M_I)$	$(1.3 \times 10^7 M_I)$	$(5.6 \times 10^6 M_I)$
$ \vec{v}_I = 30 \text{ km/s}$	LIMIT	$5.6 \times 10^{12} \text{ kg}$	$9.6 \times 10^{11} \text{ kg}$	$2.0 \times 10^{11} \text{ kg}$	$5.6 \times 10^{10} \text{ kg}$	$1.9 \times 10^{10} \text{ kg}$	$7.8 \times 10^9 \text{ kg}$
	LIMIT	$(4.7 \times 10^8 M_I)$	$(8.0 \times 10^7 M_I)$	$(1.7 \times 10^7 M_I)$	$(4.7 \times 10^6 M_I)$	$(1.6 \times 10^6 M_I)$	$(6.5 \times 10^5 M_I)$
$ \vec{v}_I = 60 \text{ km/s}$	LIMIT	$3.8 \times 10^{12} \text{ kg}$	$6.7 \times 10^{11} \text{ kg}$	$1.4 \times 10^{11} \text{ kg}$	$4.1 \times 10^{10} \text{ kg}$	$1.4 \times 10^{10} \text{ kg}$	$5.8 \times 10^9 \text{ kg}$
	LIMIT	$(3.2 \times 10^8 M_I)$	$(5.6 \times 10^7 M_I)$	$(1.2 \times 10^7 M_I)$	$(3.4 \times 10^6 M_I)$	$(1.2 \times 10^6 M_I)$	$(4.8 \times 10^5 M_I)$
$ \vec{v}_I = 100 \text{ km/s}$	LIMIT	$3.1 \times 10^{12} \text{ kg}$	$5.5 \times 10^{11} \text{ kg}$	$1.2 \times 10^{11} \text{ kg}$	$3.5 \times 10^{10} \text{ kg}$	$1.2 \times 10^{10} \text{ kg}$	$4.9 \times 10^9 \text{ kg}$
	LIMIT	$(2.6 \times 10^8 M_I)$	$(4.6 \times 10^7 M_I)$	$(1.0 \times 10^7 M_I)$	$(2.9 \times 10^6 M_I)$	$(1.0 \times 10^6 M_I)$	$(4.1 \times 10^5 M_I)$
$R_T = 100 \text{ km}$							
$ \vec{v}_I = 5 \text{ km/s}$	$3.4 \times 10^{12} \text{ kg}$	$1.0 \times 10^{13} \text{ kg}$	$2.3 \times 10^{12} \text{ kg}$	$6.3 \times 10^{11} \text{ kg}$	$2.2 \times 10^{11} \text{ kg}$	$8.6 \times 10^{10} \text{ kg}$	$4.0 \times 10^{10} \text{ kg}$
	$(2.8 \times 10^5 M_I)$	$(8.5 \times 10^5 M_I)$	$(1.9 \times 10^5 M_I)$	$(5.3 \times 10^4 M_I)$	$(1.8 \times 10^4 M_I)$	$(7200 M_I)$	$(3300 M_I)$
$ \vec{v}_I = 10 \text{ km/s}$	LIMIT	$6.8 \times 10^{14} \text{ kg}$	$1.9 \times 10^{14} \text{ kg}$	$6.5 \times 10^{13} \text{ kg}$	$2.6 \times 10^{13} \text{ kg}$	$1.2 \times 10^{13} \text{ kg}$	$6.7 \times 10^{12} \text{ kg}$
	LIMIT	$(5.7 \times 10^7 M_I)$	$(1.6 \times 10^7 M_I)$	$(5.4 \times 10^6 M_I)$	$(2.2 \times 10^6 M_I)$	$(1.0 \times 10^6 M_I)$	$(5.6 \times 10^5 M_I)$
$ \vec{v}_I = 30 \text{ km/s}$	$2.9 \times 10^{13} \text{ kg}$	$1.1 \times 10^{14} \text{ kg}$	$3.0 \times 10^{13} \text{ kg}$	$9.5 \times 10^{12} \text{ kg}$	$3.6 \times 10^{12} \text{ kg}$	$1.6 \times 10^{12} \text{ kg}$	$7.8 \times 10^{11} \text{ kg}$
	$(2.4 \times 10^6 M_I)$	$(9.2 \times 10^6 M_I)$	$(2.5 \times 10^6 M_I)$	$(7.9 \times 10^5 M_I)$	$(3.0 \times 10^5 M_I)$	$(1.3 \times 10^5 M_I)$	$(6.5 \times 10^4 M_I)$
$ \vec{v}_I = 60 \text{ km/s}$	$1.8 \times 10^{13} \text{ kg}$	$7.5 \times 10^{13} \text{ kg}$	$2.2 \times 10^{13} \text{ kg}$	$6.8 \times 10^{12} \text{ kg}$	$2.6 \times 10^{12} \text{ kg}$	$1.1 \times 10^{12} \text{ kg}$	$5.8 \times 10^{11} \text{ kg}$
	$(1.5 \times 10^6 M_I)$	$(6.3 \times 10^6 M_I)$	$(1.8 \times 10^6 M_I)$	$(5.7 \times 10^5 M_I)$	$(2.2 \times 10^5 M_I)$	$(9.5 \times 10^4 M_I)$	$(4.8 \times 10^4 M_I)$
$ \vec{v}_I = 100 \text{ km/s}$	$1.4 \times 10^{13} \text{ kg}$	$6.1 \times 10^{13} \text{ kg}$	$1.8 \times 10^{13} \text{ kg}$	$5.8 \times 10^{12} \text{ kg}$	$2.2 \times 10^{12} \text{ kg}$	$9.8 \times 10^{11} \text{ kg}$	$4.9 \times 10^{11} \text{ kg}$
	$(1.2 \times 10^6 M_I)$	$(5.1 \times 10^6 M_I)$	$(1.5 \times 10^6 M_I)$	$(4.8 \times 10^5 M_I)$	$(1.8 \times 10^5 M_I)$	$(8.2 \times 10^4 M_I)$	$(4.1 \times 10^4 M_I)$
$R_T = 10^3 \text{ km}$							
$ \vec{v}_I = 5 \text{ km/s}$	JET						
	JET						
$ \vec{v}_I = 10 \text{ km/s}$	$1.8 \times 10^{15} \text{ kg}$	$1.3 \times 10^{16} \text{ kg}$	$6.1 \times 10^{15} \text{ kg}$	$3.0 \times 10^{15} \text{ kg}$	$1.7 \times 10^{15} \text{ kg}$	$1.0 \times 10^{15} \text{ kg}$	$6.7 \times 10^{14} \text{ kg}$
	$(1.5 \times 10^5 M_I)$	$(1.1 \times 10^6 M_I)$	$(5.1 \times 10^5 M_I)$	$(2.5 \times 10^5 M_I)$	$(1.4 \times 10^5 M_I)$	$(8.4 \times 10^4 M_I)$	$(5.6 \times 10^4 M_I)$
$ \vec{v}_I = 30 \text{ km/s}$	$2.9 \times 10^{14} \text{ kg}$	$2.2 \times 10^{15} \text{ kg}$	$9.6 \times 10^{14} \text{ kg}$	$4.4 \times 10^{14} \text{ kg}$	$2.3 \times 10^{14} \text{ kg}$	$1.3 \times 10^{14} \text{ kg}$	$7.8 \times 10^{13} \text{ kg}$
	$(2.4 \times 10^4 M_I)$	$(1.8 \times 10^5 M_I)$	$(8.0 \times 10^4 M_I)$	$(3.7 \times 10^4 M_I)$	$(1.9 \times 10^4 M_I)$	$(1.1 \times 10^4 M_I)$	$(6500 M_I)$
$ \vec{v}_I = 60 \text{ km/s}$	$1.9 \times 10^{14} \text{ kg}$	$1.4 \times 10^{15} \text{ kg}$	$6.7 \times 10^{14} \text{ kg}$	$3.1 \times 10^{14} \text{ kg}$	$1.7 \times 10^{14} \text{ kg}$	$9.3 \times 10^{13} \text{ kg}$	$5.8 \times 10^{13} \text{ kg}$
	$(1.6 \times 10^4 M_I)$	$(1.2 \times 10^5 M_I)$	$(5.6 \times 10^4 M_I)$	$(2.6 \times 10^4 M_I)$	$(1.4 \times 10^4 M_I)$	$(7800 M_I)$	$(4800 M_I)$
$ \vec{v}_I = 100 \text{ km/s}$	$1.4 \times 10^{14} \text{ kg}$	$1.2 \times 10^{15} \text{ kg}$	$5.5 \times 10^{14} \text{ kg}$	$2.6 \times 10^{14} \text{ kg}$	$1.4 \times 10^{14} \text{ kg}$	$8.0 \times 10^{13} \text{ kg}$	$4.9 \times 10^{13} \text{ kg}$
	$(1.2 \times 10^4 M_I)$	$(9.9 \times 10^4 M_I)$	$(4.6 \times 10^4 M_I)$	$(2.2 \times 10^4 M_I)$	$(1.2 \times 10^4 M_I)$	$(6700 M_I)$	$(4100 M_I)$

Table 5. Same as Table 4, but for $R_I = 10^{-3}R_T$.

Cumulative escaped mass in terms of both kg and M_I							
$R_I = 10^{-3}R_T$	$Z = 2.01$	$Z = 2.5$	$Z = 3.0$	$Z = 3.5$	$Z = 4.0$	$Z = 4.5$	$Z = 5.0$
$R_T = 1 \text{ km}$							
$ \vec{v}_I = 5 \text{ km/s}$	LIMIT	LIMIT	LIMIT	LIMIT	LIMIT	$1.3 \times 10^{10} \text{ kg}$	$4.0 \times 10^9 \text{ kg}$
	LIMIT	LIMIT	LIMIT	LIMIT	LIMIT	$(1.1 \times 10^6 M_I)$	$(3.3 \times 10^5 M_I)$
$ \vec{v}_I = 10 \text{ km/s}$	LIMIT						
	LIMIT						
$ \vec{v}_I = 30 \text{ km/s}$	LIMIT						
	LIMIT						
$ \vec{v}_I = 60 \text{ km/s}$	LIMIT						
	LIMIT						
$ \vec{v}_I = 100 \text{ km/s}$	APART						
	APART						
$R_T = 10 \text{ km}$							
$ \vec{v}_I = 5 \text{ km/s}$	LIMIT	LIMIT	LIMIT	$1.3 \times 10^{13} \text{ kg}$	$3.4 \times 10^{12} \text{ kg}$	$1.1 \times 10^{12} \text{ kg}$	$4.0 \times 10^{11} \text{ kg}$
	LIMIT	LIMIT	LIMIT	$(1.1 \times 10^6 M_I)$	$(2.8 \times 10^5 M_I)$	$(8.8 \times 10^4 M_I)$	$(3.3 \times 10^4 M_I)$
$ \vec{v}_I = 10 \text{ km/s}$	LIMIT						
	LIMIT						
$ \vec{v}_I = 30 \text{ km/s}$	LIMIT	LIMIT	LIMIT	LIMIT	LIMIT	$1.9 \times 10^{13} \text{ kg}$	$7.7 \times 10^{12} \text{ kg}$
	LIMIT	LIMIT	LIMIT	LIMIT	LIMIT	$(1.6 \times 10^6 M_I)$	$(6.4 \times 10^5 M_I)$
$ \vec{v}_I = 60 \text{ km/s}$	LIMIT	LIMIT	LIMIT	LIMIT	LIMIT	$1.4 \times 10^{13} \text{ kg}$	$5.6 \times 10^{12} \text{ kg}$
	LIMIT	LIMIT	LIMIT	LIMIT	LIMIT	$(1.2 \times 10^6 M_I)$	$(4.7 \times 10^5 M_I)$
$ \vec{v}_I = 100 \text{ km/s}$	LIMIT	LIMIT	LIMIT	LIMIT	LIMIT	$1.2 \times 10^{13} \text{ kg}$	$4.9 \times 10^{12} \text{ kg}$
	LIMIT	LIMIT	LIMIT	LIMIT	LIMIT	$(9.9 \times 10^5 M_I)$	$(4.1 \times 10^5 M_I)$
$R_T = 100 \text{ km}$							
$ \vec{v}_I = 5 \text{ km/s}$	LIMIT	LIMIT	$2.3 \times 10^{15} \text{ kg}$	$6.3 \times 10^{14} \text{ kg}$	$2.2 \times 10^{14} \text{ kg}$	$8.6 \times 10^{13} \text{ kg}$	$4.0 \times 10^{13} \text{ kg}$
	LIMIT	LIMIT	$(1.9 \times 10^5 M_I)$	$(5.3 \times 10^4 M_I)$	$(1.8 \times 10^4 M_I)$	$(7200 M_I)$	$(3300 M_I)$
$ \vec{v}_I = 10 \text{ km/s}$	LIMIT	LIMIT	LIMIT	LIMIT	LIMIT	$1.2 \times 10^{16} \text{ kg}$	$6.6 \times 10^{15} \text{ kg}$
	LIMIT	LIMIT	LIMIT	LIMIT	LIMIT	$(1.0 \times 10^6 M_I)$	$(5.5 \times 10^5 M_I)$
$ \vec{v}_I = 30 \text{ km/s}$	LIMIT	LIMIT	LIMIT	$9.3 \times 10^{15} \text{ kg}$	$3.5 \times 10^{15} \text{ kg}$	$1.6 \times 10^{15} \text{ kg}$	$7.7 \times 10^{14} \text{ kg}$
	LIMIT	LIMIT	LIMIT	$(7.8 \times 10^5 M_I)$	$(2.9 \times 10^5 M_I)$	$(1.3 \times 10^5 M_I)$	$(6.4 \times 10^4 M_I)$
$ \vec{v}_I = 60 \text{ km/s}$	LIMIT	LIMIT	LIMIT	$6.7 \times 10^{15} \text{ kg}$	$2.5 \times 10^{15} \text{ kg}$	$1.1 \times 10^{15} \text{ kg}$	$5.6 \times 10^{14} \text{ kg}$
	LIMIT	LIMIT	LIMIT	$(5.6 \times 10^5 M_I)$	$(2.1 \times 10^5 M_I)$	$(9.5 \times 10^4 M_I)$	$(4.7 \times 10^4 M_I)$
$ \vec{v}_I = 100 \text{ km/s}$	LIMIT	LIMIT	LIMIT	$5.6 \times 10^{15} \text{ kg}$	$2.2 \times 10^{15} \text{ kg}$	$9.7 \times 10^{14} \text{ kg}$	$4.9 \times 10^{14} \text{ kg}$
	LIMIT	LIMIT	LIMIT	$(4.7 \times 10^5 M_I)$	$(1.8 \times 10^5 M_I)$	$(8.1 \times 10^4 M_I)$	$(4.1 \times 10^4 M_I)$
$R_T = 10^3 \text{ km}$							
$ \vec{v}_I = 5 \text{ km/s}$	JET						
	JET						
$ \vec{v}_I = 10 \text{ km/s}$	LIMIT	LIMIT	$6.0 \times 10^{18} \text{ kg}$	$3.0 \times 10^{18} \text{ kg}$	$1.7 \times 10^{18} \text{ kg}$	$9.9 \times 10^{17} \text{ kg}$	$6.6 \times 10^{17} \text{ kg}$
	LIMIT	LIMIT	$(5.0 \times 10^5 M_I)$	$(2.5 \times 10^5 M_I)$	$(1.4 \times 10^5 M_I)$	$(8.3 \times 10^4 M_I)$	$(5.5 \times 10^4 M_I)$
$ \vec{v}_I = 30 \text{ km/s}$	LIMIT	$2.2 \times 10^{18} \text{ kg}$	$9.6 \times 10^{17} \text{ kg}$	$4.4 \times 10^{17} \text{ kg}$	$2.3 \times 10^{17} \text{ kg}$	$1.3 \times 10^{17} \text{ kg}$	$7.8 \times 10^{16} \text{ kg}$
	LIMIT	$(1.8 \times 10^5 M_I)$	$(8.0 \times 10^4 M_I)$	$(3.7 \times 10^4 M_I)$	$(1.9 \times 10^4 M_I)$	$(1.1 \times 10^4 M_I)$	$(6500 M_I)$
$ \vec{v}_I = 60 \text{ km/s}$	LIMIT	$1.4 \times 10^{18} \text{ kg}$	$6.7 \times 10^{17} \text{ kg}$	$3.1 \times 10^{17} \text{ kg}$	$1.7 \times 10^{17} \text{ kg}$	$9.2 \times 10^{16} \text{ kg}$	$5.8 \times 10^{16} \text{ kg}$
	LIMIT	$(1.2 \times 10^5 M_I)$	$(5.6 \times 10^4 M_I)$	$(2.6 \times 10^4 M_I)$	$(1.4 \times 10^4 M_I)$	$(7700 M_I)$	$(4800 M_I)$
$ \vec{v}_I = 100 \text{ km/s}$	$1.4 \times 10^{17} \text{ kg}$	$1.2 \times 10^{18} \text{ kg}$	$5.5 \times 10^{17} \text{ kg}$	$2.6 \times 10^{17} \text{ kg}$	$1.4 \times 10^{17} \text{ kg}$	$7.9 \times 10^{16} \text{ kg}$	$4.9 \times 10^{16} \text{ kg}$
	$(1.2 \times 10^4 M_I)$	$(9.8 \times 10^4 M_I)$	$(4.6 \times 10^4 M_I)$	$(2.2 \times 10^4 M_I)$	$(1.2 \times 10^4 M_I)$	$(6600 M_I)$	$(4100 M_I)$

Table 6. Escaped post-collisional mass for impacts between a spherical basaltic impactor and a spherical target of different materials. See the Table 3 caption for explanations of the non-numeric entries. In all cases, $R_T = 500$ km and $R_I = 10^{-3}R_T = 0.5$ km.

Cumulative escaped mass in terms of both kg and M_I							
	$Z = 2.01$	$Z = 2.5$	$Z = 3.0$	$Z = 3.5$	$Z = 4.0$	$Z = 4.5$	$Z = 5.0$
Basaltic target							
$ \vec{v}_I = 5$ km/s	1.6×10^{16} kg ($1.1 \times 10^4 M_I$)	8.1×10^{16} kg ($5.4 \times 10^4 M_I$)	2.5×10^{16} kg ($1.7 \times 10^4 M_I$)	9.3×10^{15} kg ($6200 M_I$)	3.9×10^{15} kg ($2600 M_I$)	1.8×10^{15} kg ($1200 M_I$)	1.0×10^{15} kg ($670 M_I$)
$ \vec{v}_I = 10$ km/s	LIMIT	LIMIT	LIMIT	9.3×10^{17} kg ($6.2 \times 10^5 M_I$)	4.6×10^{17} kg ($3.1 \times 10^5 M_I$)	2.7×10^{17} kg ($1.8 \times 10^5 M_I$)	1.6×10^{17} kg ($1.1 \times 10^5 M_I$)
$ \vec{v}_I = 30$ km/s	LIMIT	LIMIT	3.3×10^{17} kg ($2.2 \times 10^5 M_I$)	1.4×10^{17} kg ($9.2 \times 10^4 M_I$)	6.3×10^{16} kg ($4.2 \times 10^4 M_I$)	3.3×10^{16} kg ($2.2 \times 10^4 M_I$)	1.9×10^{16} kg ($1.3 \times 10^4 M_I$)
$ \vec{v}_I = 60$ km/s	LIMIT	5.8×10^{17} kg ($3.9 \times 10^5 M_I$)	2.4×10^{17} kg ($1.6 \times 10^5 M_I$)	9.9×10^{16} kg ($6.6 \times 10^4 M_I$)	4.6×10^{16} kg ($3.1 \times 10^4 M_I$)	2.4×10^{16} kg ($1.6 \times 10^4 M_I$)	1.4×10^{16} kg ($9500 M_I$)
$ \vec{v}_I = 100$ km/s	LIMIT	4.8×10^{17} kg ($3.2 \times 10^5 M_I$)	1.9×10^{17} kg ($1.3 \times 10^5 M_I$)	8.4×10^{16} kg ($5.6 \times 10^4 M_I$)	3.9×10^{16} kg ($2.6 \times 10^4 M_I$)	2.1×10^{16} kg ($1.4 \times 10^4 M_I$)	1.2×10^{16} kg ($8200 M_I$)
Granite target							
$ \vec{v}_I = 5$ km/s	VAPOR						
$ \vec{v}_I = 10$ km/s	1.6×10^{16} kg ($1.1 \times 10^4 M_I$)	1.9×10^{17} kg ($1.3 \times 10^5 M_I$)	1.2×10^{17} kg ($8.1 \times 10^4 M_I$)	7.5×10^{16} kg ($5.0 \times 10^4 M_I$)	4.9×10^{16} kg ($3.3 \times 10^4 M_I$)	3.4×10^{16} kg ($2.3 \times 10^4 M_I$)	2.5×10^{16} kg ($1.7 \times 10^4 M_I$)
$ \vec{v}_I = 30$ km/s	1.5×10^{15} kg ($980 M_I$)	1.8×10^{16} kg ($1.2 \times 10^4 M_I$)	1.2×10^{16} kg ($7900 M_I$)	7.3×10^{15} kg ($4900 M_I$)	4.8×10^{15} kg ($3200 M_I$)	3.3×10^{15} kg ($2200 M_I$)	2.4×10^{15} kg ($1600 M_I$)
$ \vec{v}_I = 60$ km/s	8.5×10^{14} kg ($570 M_I$)	1.1×10^{16} kg ($7300 M_I$)	7.3×10^{15} kg ($4900 M_I$)	4.6×10^{15} kg ($3100 M_I$)	3.0×10^{15} kg ($2000 M_I$)	2.1×10^{15} kg ($1400 M_I$)	1.5×10^{15} kg ($1000 M_I$)
$ \vec{v}_I = 100$ km/s	6.6×10^{14} kg ($440 M_I$)	8.5×10^{15} kg ($5700 M_I$)	5.8×10^{15} kg ($3900 M_I$)	3.7×10^{15} kg ($2500 M_I$)	2.5×10^{15} kg ($1700 M_I$)	1.6×10^{15} kg ($1100 M_I$)	1.3×10^{15} kg ($840 M_I$)
Waterworld target							
$ \vec{v}_I = 5$ km/s	2.5×10^{11} kg ($0.17 M_I$)	4.9×10^{12} kg ($3.3 M_I$)	4.6×10^{12} kg ($3.1 M_I$)	VAPOR	VAPOR	VAPOR	VAPOR
$ \vec{v}_I = 10$ km/s	2.4×10^{13} kg ($16 M_I$)	4.9×10^{14} kg ($330 M_I$)	5.1×10^{14} kg ($340 M_I$)	4.5×10^{14} kg ($300 M_I$)	3.9×10^{14} kg ($260 M_I$)	3.4×10^{14} kg ($230 M_I$)	3.1×10^{14} kg ($210 M_I$)
$ \vec{v}_I = 30$ km/s	5.8×10^{12} kg ($3.9 M_I$)	1.2×10^{14} kg ($82 M_I$)	1.3×10^{14} kg ($89 M_I$)	9.0×10^{13} kg ($60 M_I$)	8.1×10^{13} kg ($54 M_I$)	6.9×10^{13} kg ($46 M_I$)	6.0×10^{13} kg ($40 M_I$)
$ \vec{v}_I = 60$ km/s	4.8×10^{12} kg ($3.2 M_I$)	9.6×10^{13} kg ($64 M_I$)	9.4×10^{13} kg ($63 M_I$)	8.1×10^{13} kg ($54 M_I$)	6.9×10^{13} kg ($46 M_I$)	6.1×10^{13} kg ($41 M_I$)	4.0×10^{13} kg ($27 M_I$)
$ \vec{v}_I = 100$ km/s	5.4×10^{12} kg ($3.6 M_I$)	9.9×10^{13} kg ($66 M_I$)	9.1×10^{13} kg ($61 M_I$)	7.5×10^{13} kg ($50 M_I$)	6.1×10^{13} kg ($41 M_I$)	5.2×10^{13} kg ($35 M_I$)	4.5×10^{13} kg ($30 M_I$)
Iron target							
$ \vec{v}_I = 5$ km/s	1.8×10^{14} kg ($118 M_I$)	1.8×10^{15} kg ($1200 M_I$)	1.1×10^{15} kg ($710 M_I$)	6.0×10^{14} kg ($400 M_I$)	3.7×10^{14} kg ($250 M_I$)	2.4×10^{14} kg ($160 M_I$)	VAPOR
$ \vec{v}_I = 10$ km/s	2.1×10^{16} kg ($1.4 \times 10^4 M_I$)	1.9×10^{17} kg ($1.3 \times 10^5 M_I$)	1.2×10^{17} kg ($7.9 \times 10^4 M_I$)	7.0×10^{16} kg ($4.7 \times 10^4 M_I$)	4.5×10^{16} kg ($3.0 \times 10^4 M_I$)	3.1×10^{16} kg ($2.1 \times 10^4 M_I$)	2.4×10^{16} kg ($1.6 \times 10^4 M_I$)
$ \vec{v}_I = 30$ km/s	1.1×10^{16} kg ($7300 M_I$)	1.0×10^{17} kg ($6.7 \times 10^4 M_I$)	5.4×10^{16} kg ($3.6 \times 10^4 M_I$)	2.8×10^{16} kg ($1.9 \times 10^4 M_I$)	1.6×10^{16} kg ($1.1 \times 10^4 M_I$)	9.7×10^{15} kg ($6500 M_I$)	6.4×10^{15} kg ($4300 M_I$)
$ \vec{v}_I = 60$ km/s	8.8×10^{15} kg ($5900 M_I$)	8.4×10^{16} kg ($5.6 \times 10^4 M_I$)	4.5×10^{16} kg ($3.0 \times 10^4 M_I$)	2.4×10^{16} kg ($1.6 \times 10^4 M_I$)	1.4×10^{16} kg ($9300 M_I$)	8.7×10^{15} kg ($5800 M_I$)	5.7×10^{15} kg ($3800 M_I$)
$ \vec{v}_I = 100$ km/s	7.6×10^{15} kg ($5100 M_I$)	7.5×10^{16} kg ($5.0 \times 10^4 M_I$)	4.0×10^{16} kg ($2.7 \times 10^4 M_I$)	2.2×10^{16} kg ($1.5 \times 10^4 M_I$)	1.3×10^{16} kg ($8600 M_I$)	8.1×10^{15} kg ($5400 M_I$)	5.4×10^{15} kg ($3600 M_I$)

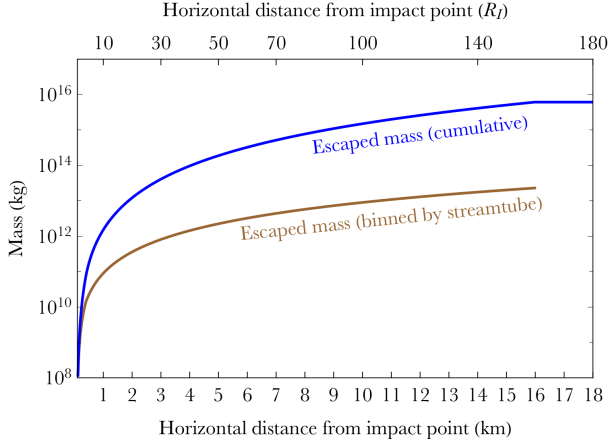


Figure 3. Demonstration of how the amount of mass per bin increases as a function of horizontal distance from the impact point, for the same impact event that is shown in Fig. 2. Due to this increase, any mass near the impact point susceptible to vaporization would be negligible compared to the cumulative mass which escapes the target.

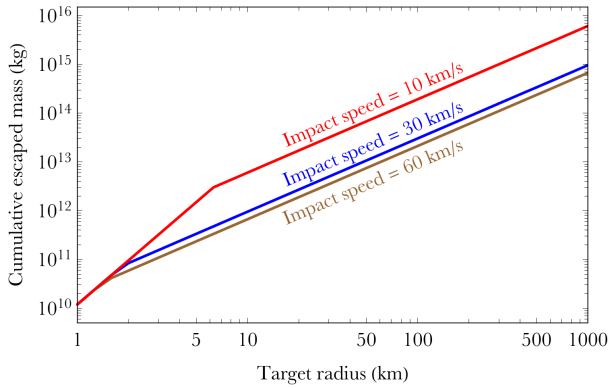


Figure 4. How the magnitude of the escaped mass varies with the target radius and impact speed, for $R_I = 10^{-4} R_T$, $Z = 3$ and basaltic impactors and targets.

dependencies of the minimum escaped mass, which are on $|\vec{v}_I|$ and R_T , and allows one to see how the result varies over the entire gamut of streamtube shape changes ($Z = 2 - 5$). In some cases, particularly in Table 5, the full-chain analytical model is applicable for only a subset of Z . The diversity of values in Tables 3-5 highlights the danger of oversimplifying the crater ejecta process across the entire phase space with just a single output.

Table 6 instead displays the magnitude of the minimum escaped mass when the impactor and target are made of different materials for $R_T = 500$ km and $R_I = 10^{-3} R_T = 5$ km⁸. The table shows that the minimum escaped mass fractions for collisions involving basalt, granite, and iron are roughly within the same order of magnitude. The significant outlier is water, for which the minimum escaped mass appears to be lower, and is the only target material for which

⁸ A basalt target and impactor is also included here, because this combination of radii is not sampled elsewhere.

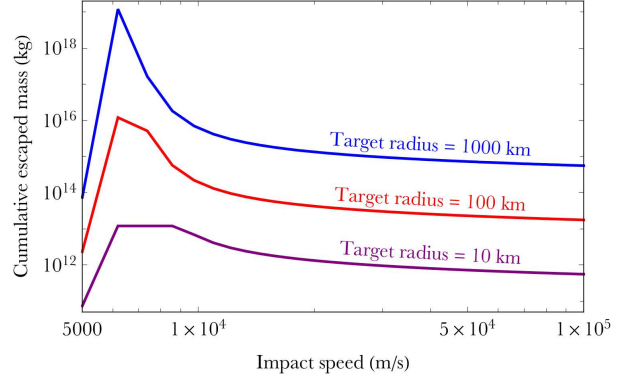


Figure 5. How the magnitude of the escaped mass varies with the impact speed and target radius, for the same system as in Fig. 4. The peak arises partly because of the impact speed-dependent functional form of n in equation (4).

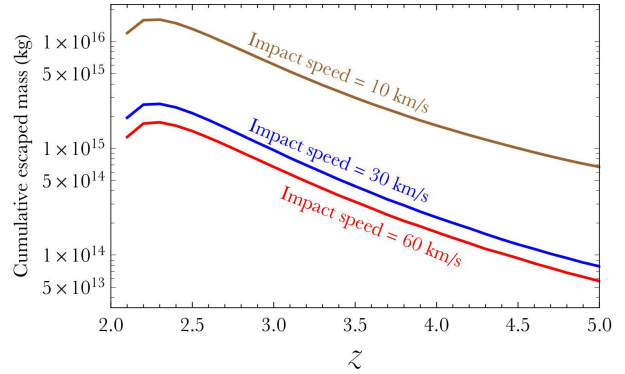


Figure 6. How the magnitude of the escaped mass varies with the entire range of Z (streamtube shape) and impact speed, for $R_T = 10^3$ km, $R_I = 10^{-4} R_T$ and basaltic impactors and targets.

the minimum escaped mass does not exceed the impactor mass (but in one case only).

Figs. 2-6 help illustrate the dependencies of various variables on minimum escaped mass for selected impact scenarios. Excavated mass cannot escape the target unless its speed exceeds the escape speed (Fig. 2). The mass which escapes contains an excess speed that is well above the escape speed in all cases except for a narrow band of D (representing about 2.5 km in the figure, or about 15 per cent of the distance to the impact point). The location where the escape and ejecta speeds are equal (at about $D = 16$ km) signals the furthest distance from the impact point where material escapes the target.

For the same system, Fig. 3 illustrates the mass loss profile. The lower brown line represents the escaped mass binned by streamtube, which monotonically increases until the cutoff point (where material stops escaping). This monotonic increase demonstrates that most of the mass which escapes occurs far from the impact point: at many tens of R_I (upper x -axis). The consequences are that any vaporization which occurs within a few R_I would provide a negligible contribution to the cumulative escaped mass.

Figures 4 and 5 reveal largely linear dependencies on log-log scales of the escaped mass on both the target radius and impact speed, at least for the basaltic $R_I = 10^{-4} R_T$

and $Z = 3$ case. However, the dependence of escaped mass on Z is not as obvious, as indicated by Fig. 6. The figure illustrates that the escaped mass can vary by several orders of magnitude across all values of Z , with the greatest escaping mass occurring for a Z value between 2.0 and 2.5. This trend is largely consistent with the impact scenarios presented across Tables 3-6.

5 OBSERVATIONAL CONSTRAINTS

Unless observations of a white dwarf planetary system fortuitously happen to coincide with an intra-system collision (Bear & Soker 2013; Wang et al. 2019), what we actually would see is the aftermath. The endstate for much of the debris ejecta – after being slowly radiatively dragged towards the white dwarf – will be accretion onto its photosphere. These metal pollution signatures are observed in abundance (see Section 1.1.1). Hence, the salient question is, can the post-collision debris be seen either in place or en route to the white dwarf?

Most dust around white dwarfs is found within the star’s disruption, or Roche, radius in the form of compact rings or discs (Farihi 2016; Manser et al. 2020). These structures do not necessarily arise from radially drifting debris, but instead could be formed by the destruction of exo-asteroids which veer into (Graham et al. 1990; Jura 2003; Debes et al. 2012; Veras et al. 2014c; Malamud & Perets 2020a) or close to (Makarov & Veras 2019; Veras et al. 2020a) the Roche radius at about 0.005 au. Further, any particles sublimated off a volatile-rich planetesimal would occur around the Roche radius (Stone et al. 2015; Veras et al. 2015c; van Lieshout et al. 2018). Therefore, observationally testing the efficacy of the impact mechanism would require observations of dust which reside at a distance that is beyond several times the white dwarf Roche radius.

Mid-IR observations represent a possible probe of this region because of the wavelengths at which dust emits. The upper limits to 20-30 micron flux observations rule out significant influxes of dust from larger separations, as would be expected for dust being fed by collisions between minor planets. Hence, these observations are important, but unfortunately at this time are sparse. Farihi et al. (2014) placed limits on the dust mass in the G29-38 planetary system as a function of dust temperature. They showed that at, for example, a distance of about 11 au, the dust mass cannot be higher than that of Haumea (3×10^{21} kg). Another system with constraints is GD 362: Xu et al. (2013) established limits on the dust mass ($10^{22} - 10^{26}$ kg) for separations ranging between 5-30 au.

The lack of (a substantial amount of) cold dust in these two systems at distances of several to tens of au suggests that a distant collision event with ejecta mass exceeding that of the largest minor planets in the solar system has not occurred recently (relative to the white dwarf cooling ages). However, if metal pollution primarily arises from bodies smaller than Haumea, then these mass limits might be too high to produce useful constraints. These systems also represent only about 0.2 per cent of all known polluted white dwarf systems. Therefore, although we cannot make any sweeping conclusions about the efficacy of the impact mechanism for producing pollutants by using these constraints,

we certainly appeal for additional observations of cold dust in polluted white dwarf planetary systems.

6 POSSIBLE SCENARIOS

Collisions can occur anywhere within white dwarf planetary systems: both near the white dwarf Roche radius at 0.005 au and at distances of 100 au. The computations we have provided here in Tables 3-6 can be applied across this entire range. Now we outline two possible scenarios in which the results of this paper may be used.

6.1 Cool white dwarf with asteroid on compact orbit

The minor planet or planets orbiting WD 1145+017 are detectable because they are close enough to the white dwarf (with a separation of approximately 0.005 au) to be breaking up and producing transiting debris. If, however, a 10^3 km-radius minor planet was slightly further away from the white dwarf, at a distance of say, 0.5 au (similar to the semimajor axis of the debris orbiting ZTF J0139+5245; Vanderbosch et al. 2019), then it would not be disrupted and could be hidden from view (van Sluijs & van Eylen 2018).

This 10^3 km-radius minor planet would be too large to be radiatively dragged towards the white dwarf, which we take to have a cooling age of 3 Gyr (similar to the age of LSPM J0207+3331, which has reported infrared excesses; Debes et al. 2019). Hence, this large minor planet is dynamically stagnant: not detectable, and not polluting the white dwarf.

Suppose further that the mass reservoirs in the outer planetary system (say at around 5 au) are not suited to produce the type of dynamical encounters envisaged by the canonical model for pollution: In other words, the major planet or planets at this distance cannot perturb a pool of smaller 1 km-radius asteroids (at around 5 au) onto orbits which graze the white dwarf Roche radius (at 0.005 au), nor even reach three times this distance, where breakup could occur (Makarov & Veras 2019; Veras et al. 2020a). The eccentricity required to reach 0.015 au from 5 au would be about 0.997.

Failure to achieve this eccentricity would mean that the white dwarf would never be metal polluted. However, if these small 1 km-radius minor planets at 5 au are perturbed more gently, to achieve significantly less eccentric orbits (with eccentricities of just about 0.9), then they could collide with the 10^3 km-radius minor planet at 0.5 au.

If we assume that both the target and impactor are basaltic, then we can use Table 5 to characterize the collision. We estimate that the collision speed is about 60 km/s from equation (3), meaning that we would read across the corresponding row in the bottommost section of Table 5.

We find that depending on the geometry adopted, about $10^{17} - 10^{18}$ kg of ejecta mass would be produced in a single collision. This amount well exceeds the impactor mass by many orders of magnitude. This ejecta mass is now available to pollute the white dwarf. Even though the white dwarf is cool at 3 Gyr old, its radiation would drag inwards dust and

pebbles at 0.5 au, even those on highly eccentric orbits. Although the pollution timescale would be a detailed function of both the geometry of the collision and the size distribution of the crater ejecta, we can estimate from Veras et al. (2015b) that the debris would pollute the white dwarf within a few orders of magnitude of Myrs. Also, during this period, other collisions with the original target might occur, making available additional potentially polluting debris.

6.2 Hot white dwarf with asteroid on wide orbit

Now consider a completely different scenario. Suppose a hot white dwarf has the same 13 Myr cooling age as WD J0914+1914 (Gänsicke et al. 2019) and hosts a series of planets and asteroids which all have semimajor axes and orbital pericentres beyond 10 au. Hence the region between the white dwarf photosphere and 10 au is clear of material. Further assume that there is no future prospect of the minor planets being perturbed within this boundary.

In this case, the white dwarf would never be polluted, and also give no indication of the planetary system which it hosts. Suppose, however, that a 500 km-radius iron core resides at a distance of 20 au and is smashed into by a collection of 0.5 km-radius basaltic impactors. Hence, we use Table 6 to model these collisions. At this separation, a likely collision speed is 5 km/s. For this speed, the bottommost portion of the table indicates that while some of the ejecta is vaporized, a single collision will generally produce about $10^{14} - 10^{15}$ kg of debris.

This debris is now available to pollute the white dwarf. Because the white dwarf is so young and luminous (with a luminosity of about a tenth of the Sun's), it can drag this debris into its photosphere, even from distances of tens of au. The drag timescale is again dependent on the geometry of the collision and the size distribution assumed for the debris, but roughly can occur on Myr timescales.

7 DISCUSSION

The results in this paper can be used to help constrain dynamical models of planetary system evolution which lead to polluted white dwarfs. Despite the mounting observations of planetary debris in a white dwarf's immediate circumstellar environment (see Section 1.1), understanding the dynamical history of these systems remains an important but largely outstanding task. Current treatments which involve only dynamical interactions between major and minor planets as pollution sources may be too simplistic.

Debris in the interplanetary environment represents another pathway for metal pollution, particularly in cases when exo-asteroids themselves are rarely perturbed towards the white dwarf, or perturbed towards the white dwarf only in concentrated periods of time (which are unlikely to be observed). As shown here, a net gain of interplanetary debris can easily be generated by a single collision on an atmosphere-less target; these targets are likely to be common in white dwarf planetary systems subsequent to the evaporative effects of the progenitor star.

Debris-producing collisions can be generated from gravitational instabilities amongst the extant objects (which likely involve at least one major planet) on short or long

timescales, as well as from stellar flybys. Hence, considering impact debris in white dwarf planetary systems which experience bombardments from Nice-model like events may be important. Subsequently, an analysis of the impact geometry, escape geometry, and speed of the debris coupled with gravitational perturbations and radiative drag forces can yield time-dependent mass and size distributions, as well as chemical composition information based on impactor and target materials.

This information may be fed into various models, such as, for example, those from Wyatt et al. (2014), Brown et al. (2017) and Kenyon & Bromley (2017a,b), to obtain a more accurate population synthesis. Wyatt et al. (2014) constrained the mass distribution of accreted material from observed atmospheric pollution, and considered stochastic and continuous accretion regimes. Brown et al. (2017) provided formulae which determine if debris that is steeply infalling into a white dwarf will be sublimated, fragmented or impacted onto the stellar photosphere. Kenyon & Bromley (2017a) and Kenyon & Bromley (2017b) utilised collisional cascades to model white dwarf debris discs, and incorporated inflow from the circumstellar environment.

Establishing a compositional link between crater ejecta and metals found in white dwarfs is another important extension of these results. If observational distinctions between detections of the bulk remains of an exo-asteroid versus the crustal material of an exo-planet can be enhanced (Harrison et al. 2018; Hollands et al. 2018; Bonsor et al. 2020), then understanding the mass and dynamical pathways of impact ejecta would become more important. Tracing the chemistry and dynamics back to planetary system formation along the early main sequence phase (Harrison et al. 2018; Bonsor et al. 2020) has the potential to link planetary architecture with instabilities, bombardments and observed accretion rates.

The impact crater formalism developed in Kurosawa & Takada (2019) and used here provides a fully analytical alternative to the π -group scaling laws (Holsapple & Schmidt 1982), which require resource-consuming experimental work to obtain empirical constants across the phase space. The flexibility and speed of the Kurosawa & Takada (2019) formalism facilitates the study of white dwarf planetary systems because of their potential to harbour a wide variety of objects and architectures. Extending the formalism to account for very high speed impacts (> 100 km/s) and objects of high internal strength could then be applicable to impacts which occur just outside the white dwarf Roche radius, and for objects like the high-strength exo-asteroid discovered by Manser et al. (2019). Because tidal interactions can quickly alter orbits (Veras et al. 2019b; Veras & Wolszczan 2019; Veras & Fuller 2019, 2020), the same target might experience different impact regimes over short timescales relative to the white dwarf cooling age.

Further, if the magnitude of the vaporized mass represented a non-negligible fraction of the escaped ejecta mass, then the temperature of the target and the white dwarf cooling age would have been important considerations. However, the independence of these variables suggest that the results in this paper may be applied to exoplanetary systems with any type of star. The implications of debris generation for giant branch planetary systems are just as important, par-

ticularly for the material which survives to the white dwarf phase (and is eventually observable there).

8 SUMMARY

We have quantitatively introduced the idea that metal pollution in some white dwarf atmospheres may be due in part or in full to post-impact debris rather than solely the ingestion of entire asteroids, comets or moons. Hence, white dwarf planetary systems where minor planets do not have a dynamical pathway to reach the central star themselves can nevertheless feature a polluted white dwarf because of collisional ejecta following bombardment events. We utilised the full-chain analytical impact crater model of Kurosawa & Takada (2019) to compute lower bounds on the ejecta mass which escapes the gravitational pull of an atmosphere-less target subsequent to a single collision. Our applications spanned a range of impact speeds (5-100 km/s), target radii (10^{0-3} km) and chemical compositions (basalt, granite, water, iron) which are either known or expected to exist in white dwarf planetary systems. We report our minimum escape estimates in Tables 3-6, which provide values that can constrain future dynamical modelling studies. Our results may be applied within any exo-planetary system, not just those containing white dwarfs.

ACKNOWLEDGEMENTS

We thank an anonymous reviewer and Boris Ivanov for valuable comments which have greatly improved the manuscript. DV gratefully acknowledges the support of the STFC via an Ernest Rutherford Fellowship (grant ST/P003850/1), and funding from the University of Warwick's Habitability Global Research Priorities (GRP) Programme. KK is supported by JSPS KAKENHI grant numbers JP17H01176, JP17H01175, JP17K18812, JP17H02990, JP18HH04464, JP19H00726 and by the Astrobiology Center of the National Institute of Natural Sciences, NINS (AB301018). We also acknowledge useful initial discussions at the 9th Workshop on Catastrophic Disruption in the Solar System in Kobe.

REFERENCES

- Ahrens, T. J., & O'Keefe, J. D. 1972, *The Moon*, 4, 214
 Alcock, C., Fristrom, C. C., & Siegelman, R. 1986, *ApJ*, 302, 462
 Anderson, J. L. B., Schultz, P. H., & Heineck, J. T. 2003, *Journal of Geophysical Research (Planets)*, 108, 5094
 Anderson, J. L. B., Schultz, P. H., & Heineck, J. T. 2004, *Meteoritics and Planetary Science*, 39, 30
 Andrews, S. M. 2020, *ARA&A In Press*, arXiv:2001.05007
 Ang, J. A. 1990, *International Journal of Impact Engineering*, 10, 23.
 Artemieva, N., & Ivanov, B. 2004, *Icarus*, 171, 84
 Artemieva, N. A., & Shuvalov, V. V. 2008, *Solar System Research*, 42, 329.
 Bear, E., & Soker, N. 2011, *MNRAS*, 414, 1788
 Bear, E., & Soker, N. 2013, *New Astronomy*, 19, 56
 Bear, E., & Soker, N. 2015, *MNRAS*, 450, 4233
 Bierhaus M., Noack L., Wünnemann K., Breuer D., 2013, *LPSC*, 2420
 Bodman, E. H. L., Wright, J. T., Desch, S. J., et al. 2018, *AJ*, 156, 173
 Bonsor, A., & Wyatt, M. 2010, *MNRAS*, 409, 1631
 Bonsor, A., Kennedy, G. M., Crepp, J. R., et al. 2013, *MNRAS*, 431, 3025
 Bonsor, A., Kennedy, G. M., Wyatt, M. C., Johnson, J. A., & Sibthorpe, B. 2014, *MNRAS*, 437, 3288
 Bonsor, A., & Veras, D. 2015, *MNRAS*, 454, 53
 Bonsor, A., Carter, P. J., Hollands, M., et al. 2020, *MNRAS*, 492, 2683
 Brown, J. C., Veras, D., & Gänsicke, B. T. 2017, *MNRAS*, 468, 1575
 Burchell, M. J., & Mackay, N. G. 1998, *JGR*, 103, 22761
 Cabral, N., Lagarde, N., Reylé, C., et al. 2019, *A&A*, 622, A49
 Caiazzo, I., & Heyl, J. S. 2017, *MNRAS*, 469, 2750
 Campbell, B., Walker, G. A. H., & Yang, S. 1988, *ApJ*, 331, 902
 Cauley, P. W., Farihi, J., Redfield, S., et al. 2018, *ApJL*, 852, L22
 Cintala, M. J., Berthoud, L., & Hörz, F. 1999, *Meteoritics and Planetary Science*, 34, 605.
 Colón, K. D., Zhou, G., Shporer, A., et al. 2018, *AJ*, 156, 227
 Coutu, S., Dufour, P., Bergeron, P., et al. 2019, arXiv:1907.05932
 Croft, S. K. 1980, *Lunar and Planetary Science Conference Proceedings*, 3, 2347.
 de Sousa Ribeiro, R., Morbidelli, A., Raymond, S. N., Izidoro, A., Gomes R., Vieira Neto, E. 2020, *Icarus*, 339, 113605
 Debes, J. H., & Sigurdsson, S. 2002, *ApJ*, 572, 556
 Debes, J. H., Walsh, K. J., & Stark, C. 2012, *ApJ*, 747, 148
 Debes, J. H., Thévenot, M., Kuchner, M. J., et al. 2019, *ApJL*, 872, L25
 DeCarli, P. S., El Goresy, A., Xie, Z., et al. 2007, *Shock Compression of Condensed Matter*, 1371.
 DeCarli, P. S. 2013, *Proc. Eng.* 58, 570
 Dong, R., Wang, Y., Lin, D. N. C., & Liu, X.-W. 2010, *ApJ*, 715, 1036
 Doyle, A. E., Young, E. D., Klein, B., et al. 2019, *Science*, 366, 356
 Dufour, P., Bergeron, P., Liebert, J., et al. 2007, *ApJ*, 663, 1291
 Dufour, P., Kilic, M., Fontaine, G., et al. 2012, *ApJ*, 749, 6
 Farihi, J., Gänsicke, B. T., & Koester, D. 2013, *Science*, 342, 218
 Farihi, J., Wyatt, M. C., Greaves, J. S., et al. 2014, *MNRAS*, 444, 1821
 Farihi, J. 2016, *New Astronomy Reviews*, 71, 9
 Fortin-Archambault, M., Dufour, P., & Xu, S. 2020, *ApJ*, 888, 47
 Gänsicke, B. T., Koester, D., Farihi, J., et al. 2012, *MNRAS*, 424, 333
 Gänsicke, B. T., Schreiber, M. R., Toloza, O., et al. 2019, *Nature*, 576, 61
 Gentile Fusillo, N. P., Gänsicke, B. T., & Greiss, S. 2015, *MNRAS*, 448, 2260
 Gentile Fusillo, N. P., Gänsicke, B. T., Farihi, J., et al.

- 2017, MNRAS, 468, 971
- Goldstein, J. 1987, A&A, 178, 283
- Gomes, R., Levison, H. F., Tsiganis, K., & Morbidelli, A. 2005, Nature, 435, 466
- Graham, J. R., Matthews, K., Neugebauer, G., et al. 1990, ApJ, 357, 216
- Greenstreet, S., Gladman, B., & McKinnon, W. B. 2015, Icarus, 258, 267.
- Grey, I. D. S., Burchell, M. J., & Shrine, N. R. G. 2002, Journal of Geophysical Research (Planets), 107, 5076
- Grishin, E., & Veras, D. 2019, MNRAS, 489, 168
- Hamers, A. S., & Portegies Zwart, S. F. 2016, MNRAS, 462, L84
- Harrison, J. H. D., Bonsor, A., & Madhusudhan, N. 2018, MNRAS, 479, 3814
- Head, J. N., Melosh, H. J., & Ivanov, B. A. 2002, Science, 298, 1752.
- Hinkel, N. R., & Unterborn, C. T. 2018, ApJ, 853, 83
- Hollands, M. A., Koester, D., Alekseev, V., Herbert, E. L., & Gänsicke, B. T. 2017, MNRAS, 467, 4970
- Hollands, M. A., Gänsicke, B. T., & Koester, D. 2018, MNRAS, 477, 93
- Holsapple, K. A., & Schmidt, R. M. 1982, JGR, 87, 1849
- Housen, K. R., Schmidt, R. M., & Holsapple, K. A. 1983, Journal of Geophysical Research, 88, 2485.
- Housen, K. R., & Holsapple, K. A. 2011, Icarus, 211, 856.
- Ito, T., & Malhotra, R. 2006, Advances in Space Research, 38, 817.
- Johnson, B. C., Bowling, T. J., & Melosh, H. J. 2014, Icarus, 238, 13.
- Johnson, B. C., Minton, D. A., Melosh, H. J., et al. 2015, Nature, 517, 339.
- Jura, M. 2003, ApJL, 584, L91
- Jura, M., Xu, S., Klein, B., Koester, D., & Zuckerman, B. 2012, ApJ, 750, 69
- Jura, M., & Young, E. D. 2014, Annual Review of Earth and Planetary Sciences, 42, 45
- Kepler, S. O., Pelisoli, I., Koester, D., et al. 2015, MNRAS, 446, 4078
- Kepler, S. O., Pelisoli, I., Koester, D., et al. 2016, MNRAS, 455, 3413
- Kenyon, S. J., & Bromley, B. C. 2017a, ApJ, 844, 116
- Kenyon, S. J., & Bromley, B. C. 2017b, ApJ, 850, 50
- Kieffer, S. W. 1977, Impact and Explosion Cratering: Planetary and Terrestrial Implications, 751.
- Klein, B., Jura, M., Koester, D., Zuckerman, B., & Melis, C. 2010, ApJ, 709, 950
- Klein, B., Jura, M., Koester, D., & Zuckerman, B. 2011, ApJ, 741, 64
- Kleinman, S. J., Kepler, S. O., Koester, D., et al. 2013, ApJS, 204, 5
- Koester, D. 2009, A&A, 498, 517
- Koester, D., Gänsicke, B. T., & Farihi, J. 2014, A&A, 566, A34
- Kostov, V. B., Moore, K., Tamayo, D., Jayawardhana, R., & Rinehart, S. A. 2016, ApJ, 832, 183
- Kozakis, T., Kaltenegger, L., & Hoard, D. W. 2018, ApJ, 862, 69
- Kral, Q., Clarke, C., & Wyatt, M. C. 2018, Handbook of Exoplanets, 165
- Kratter, K. M., & Perets, H. B. 2012, ApJ, 753, 91
- Krijt, S., Bowling, T. J., Lyons, R. J., et al. 2017, ApJ, 839, L21.
- Kunitomo, M., Guillot, T., Ida, S., et al. 2018, A&A, 618, A132
- Kurosawa, K., Nagaoka, Y., Senshu, H., et al. 2015, Journal of Geophysical Research (Planets), 120, 1237.
- Kurosawa, K., Okamoto, T., & Genda, H. 2018, Icarus, 301, 219.
- Kurosawa, K. & Takada, S. 2019, Icarus, 317, 135
- Lingam, M., & Loeb, A. 2017, Proceedings of the National Academy of Science, 114, 6689.
- Liu, F., Yong, D., Asplund, M., et al. 2018, A&A, 614, A138
- Livio, M., & Soker, N. 1984, MNRAS, 208, 763
- Makarov, V. & Veras, D. 2019, ApJ, 886, 127
- Malamud, U., & Perets, H. B. 2016, ApJ, 832, 160
- Malamud, U., & Perets, H. B. 2017a, ApJ, 842, 67
- Malamud, U., & Perets, H. B. 2017b, ApJ, 849, 8
- Malamud, U., & Perets, H. B. 2020a, MNRAS 492, 5561
- Malamud, U., & Perets, H. B. 2020b, MNRAS In Press, arXiv:1911.12184
- Manser, C. J. et al. 2019, Science, 364, 66
- Manser, C. J., Gänsicke, B. T., Gentile Fusillo, N. P., et al. 2020, MNRAS In Press, arXiv:2002.01936
- Marchi S., Bottke W. F., Elkins-Tanton L. T., Bierhaus M., Wuennemann K., Morbidelli A., Kring D. A., 2014, Natur, 511, 578
- Marcus, A. H. 1969, Icarus, 11, 76.
- Martin, R. G., Livio, M., Smallwood, J. L., et al. 2020, MNRAS In Press, arXiv:2002.04751
- Maxwell, D. E. 1977, In: Impact and Explosion Cratering. Eds: Roddy, D.J., Pepin, R.O., Merrill, R.B., Pergamon Press, Printed in the USA, pgs. 1003-1008
- Melis, C., & Dufour, P. 2017, ApJ, 834, 1
- Melosh, H. J. 1984, Icarus, 59, 234.
- Melosh, H. J. 1985a, Geology, 13, 144.
- Melosh, H. J. 1985b, Icarus, 62, 339.
- Melosh, H. J., & Sonett, C. P. 1986, Origin of the Moon, 621.
- Melosh, H. J. 1988, Nature, 332, 687.
- Melosh, H. J. 1989, New York : Oxford University Press ; Oxford : Clarendon Press
- Melosh, H. J. 2003, Astrobiology, 3, 207.
- Melosh, H. J. 2011 Planetary Surface Processes, Cambridge University Press, Cambridge UK.
- Morbidelli, A., Nesvorny, D., Laurenz, V., et al. 2018, Icarus, 305, 262
- Movshovitz, N., Nimmo, F., Korycansky, D. G., Asphaug, E., & Owen, J. M. 2016, Icarus, 275, 85
- Mustill, A. J., Marshall, J. P., Villaver, E., et al. 2013, MNRAS, 436, 2515
- Mustill, A. J., Veras, D., & Villaver, E. 2014, MNRAS, 437, 1404
- Mustill, A. J., Villaver, E., Veras, D., Gänsicke, B. T., & Bonsor, A. 2018, MNRAS, 476, 3939
- Nelemans, G., & Tauris, T. M. 1998, A&A, 335, L85
- O'Brien, D. P., & Sykes, M. V. 2011, Space Science Reviews, 163, 41.
- Okeefe, J. D., & Ahrens, T. J. 1977, Science, 198, 1249.
- Paquette, C., Pelletier, C., Fontaine, G., & Michaud, G. 1986, ApJS, 61, 197
- Parriott, J., & Alcock, C. 1998, ApJ, 501, 357

- Payne, M. J., Veras, D., Holman, M. J., Gänsicke, B. T. 2016, *MNRAS*, 457, 217
- Payne, M. J., Veras, D., Gänsicke, B. T., & Holman, M. J. 2017, *MNRAS*, 464, 2557
- Petrovich, C., & Muñoz, D. J. 2017, *ApJ*, 834, 116
- Pierazzo, E., Vickery, A. M., & Melosh, H. J. 1997, *Icarus*, 127, 408
- Pierazzo, E., & Melosh, H. J. 2000a, *Icarus*, 145, 252
- Pierazzo, E., & Melosh, H. J. 2000b, *Meteoritics and Planetary Science*, 35, 117
- Polanskey, C. A., & Ahrens, T. J. 1990, *Icarus*, 87, 140.
- Portegies Zwart, S. 2013, *MNRAS*, 429, L45
- Raddi, R., Gänsicke, B. T., Koester, D., et al. 2015, *MNRAS*, 450, 2083
- Reach, W. T., Kuchner, M. J., von Hippel, T., et al. 2005, *ApJL*, 635, L161
- Reach, W. T., Lisse, C., von Hippel, T., et al. 2009, *ApJ*, 693, 697
- Ridden-Harper, A. R., Snellen, I. A. G., Keller, C. U., et al. 2019, Submitted to *A&A*, arXiv:1906.08795
- Santos, N. C., Adibekyan, V., Dorn, C., et al. 2017, *A&A*, 608, A94
- Schatzman, E. L. 1958, Amsterdam, North-Holland Pub. Co.; New York, Interscience Publishers, 1958
- Schreiber, M. R., Gänsicke, B. T., Toloza, O., et al. 2019, *ApJL*, 887, L4
- Schröder, K.-P., & Smith, R. 2008, *MNRAS*, 386, 155
- Schultz, P. H. 1996, *JGR*, 101, 21117
- Schultz, P. H., & Wrobel, K. E. 2012, *Journal of Geophysical Research (Planets)*, 117, E04001
- Shoemaker, E. M., 1962, in *Physics and Astronomy of the Moon* (edited by Z. Kopal), Academic Press, New York and London, pp. 283-359
- Soker, N. 1998, *AJ*, 116, 1308
- Spiegel, D. S., & Madhusudhan, N. 2012, *ApJ*, 756, 132
- Stephan, A. P., Naoz, S., & Zuckerman, B. 2017, *ApJL*, 844, L16
- Stephan, A. P., Naoz, S., & Gaudi, B. S. 2018, *AJ*, 156, 128
- Stone, N., Metzger, B. D., & Loeb, A. 2015, *MNRAS*, 448, 188
- Sugita, S., & Schultz, P. H. 1999, *Journal of Geophysical Research*, 104, 30825.
- Swan, A., Farihi, J., Koester, D., et al. 2019, *MNRAS*, 490, 202
- Takizawa, S., & Katsuragi, H. 2019, arXiv:1904.11636
- Tsujido, S., Arakawa, M., Suzuki, A. I., et al. 2015, *Icarus*, 262, 79.
- van Lieshout, R., Min, M., & Dominik, C. 2014, *A&A*, 572, A76
- van Lieshout, R., Kral, Q., Charnoz, S., et al. 2018, *MNRAS*, 480, 2784
- Vanderbosch, Z., Hermes, J. J., Dennihy, E., et al. 2019, submitted to *ApJL*, arXiv:1908.09839
- Vanderburg, A., Johnson, J. A., Rappaport, S., et al. 2015, *Nature*, 526, 546
- van Sluijs, L., & Van Eylen, V. 2018, *MNRAS*, 474, 4603
- Veras, D., & Tout, C. A. 2012, *MNRAS*, 422, 1648
- Veras, D., Mustill, A. J., Bonsor, A., & Wyatt, M. C. 2013, *MNRAS*, 431, 1686
- Veras, D., Shannon, A., Gänsicke, B. T. 2014a, *MNRAS*, 445, 4175
- Veras, D., Jacobson, S. A., Gänsicke, B. T. 2014b, *MNRAS*, 445, 2794
- Veras, D., Leinhardt, Z. M., Bonsor, A., Gänsicke, B. T. 2014c, *MNRAS*, 445, 2244
- Veras, D., Gänsicke, B. T. 2015, *MNRAS*, 447, 1049
- Veras, D., Eggl, S., Gänsicke, B. T. 2015a, *MNRAS*, 451, 2814
- Veras, D., Leinhardt, Z. M., Eggl, S., Gänsicke, B. T. 2015b, *MNRAS*, 451, 3453
- Veras, D., Eggl, S., & Gänsicke, B. T. 2015c, *MNRAS*, 452, 1945
- Veras, D. 2016a, *MNRAS*, 463, 2958
- Veras, D. 2016b, *Royal Society Open Science*, 3, 150571
- Veras, D., Mustill, A. J., Gänsicke, B. T., et al. 2016, *MNRAS*, 458, 3942
- Veras, D., Georgakarakos, N., Dobbs-Dixon, I., & Gänsicke, B. T. 2017a, *MNRAS*, 465, 2053
- Veras, D., Carter, P. J., Leinhardt, Z. M., & Gänsicke, B. T. 2017b, *MNRAS*, 465, 1008
- Veras, D., Georgakarakos, N., Gänsicke, B. T., et al. 2018a, *MNRAS*, 481, 2180
- Veras, D., Armstrong, D. J., Blake, J. A., et al. 2018b, *Astrobiology*, 18, 1106
- Veras, D., Efroimsky, M., Makarov, V. V., et al. 2019b, *MNRAS*, 486, 3831
- Veras, D., Higuchi, A., & Ida, S. 2019a, *MNRAS*, 485, 708
- Veras, D., & Fuller, J. 2019, *MNRAS*, 489, 2941
- Veras, D., & Wolszczan, A. 2019, *MNRAS*, 488, 153
- Veras, D., & Fuller, J. 2020, *MNRAS* 492, 6059
- Veras, D., & Scheeres, D. J. 2020, *MNRAS*, 492, 2437
- Veras, D., McDonald, C. H., & Makarov, V. V. 2020a, *MNRAS*, 269
- Veras, D., Tremblay, P.-E., Hermes, J. J., et al. 2020b, *MNRAS*, 268
- Vickery, A. M. 1993, *Icarus*, 105, 441.
- Vickery, A. M., & Melosh, H. J. 1987, *Science*, 237, 738.
- Villaver, E., & Livio, M. 2007, *ApJ*, 661, 1192
- Voyatzis, G., Hadjidemetriou, J. D., Veras, D., & Varvoglis, H. 2013, *MNRAS*, 430, 3383
- Wang, T.-G., Jiang, N., Ge, J., et al. 2019, submitted to *ApJL*, arXiv:1910.04314
- Wickramasinghe, D. T., Farihi, J., Tout, C. A., Ferrario, L., & Stancliffe, R. J. 2010, *MNRAS*, 404, 1984
- Wilson, D. J., Gänsicke, B. T., Koester, D., et al. 2014, *MNRAS*, 445, 1878
- Wilson, D. J., Gänsicke, B. T., Koester, D., et al. 2015, *MNRAS*, 451, 3237
- Wilson, D. J., Gänsicke, B. T., Farihi, J., & Koester, D. 2016, *MNRAS*, 459, 3282
- Wyatt, M. C. 2008, *ARA&A*, 46, 339
- Wyatt, M. C., Farihi, J., Pringle, J. E., & Bonsor, A. 2014, *MNRAS*, 439, 3371
- Xu, S., Jura, M., Klein, B., Koester, D., & Zuckerman, B. 2013, *ApJ*, 766, 132
- Xu, S., Jura, M., Koester, D., Klein, B., & Zuckerman, B. 2014, *ApJ*, 783, 79
- Xu, S., Jura, M., Dufour, P., et al. 2016, *ApJL*, 816, L22
- Xu, S., Zuckerman, B., Dufour, P., et al. 2017, *ApJL*, 836, L7
- Xu, S., Dufour, P., Klein, B., et al. 2019, *AJ*, 158, 242
- Yamamoto, S., Hasegawa, S., Suzuki, A. I., et al. 2017, *Journal of Geophysical Research (Planets)*, 122, 1077

- Zuckerman, B., Koester, D., Reid, I. N., Hünsch, M. 2003, ApJ, 596, 477
- Zuckerman, B., Melis, C., Klein, B., Koester, D., & Jura, M. 2010, ApJ, 722, 725
- Zuckerman, B., & Young, E. D. 2018, Handbook of Exoplanets, 14